



HAL
open science

Astronomical pacing of Late Cretaceous third- and second-order sea-level sequences in the Foz do Amazonas Basin

Slah Boulila, Célia Brange, Alberto Machado Cruz, Jacques Laskar, Christian Gorini, Tadeu Dos Reis, Cleverson Guizan Silva

► To cite this version:

Slah Boulila, Célia Brange, Alberto Machado Cruz, Jacques Laskar, Christian Gorini, et al.. Astronomical pacing of Late Cretaceous third- and second-order sea-level sequences in the Foz do Amazonas Basin. *Marine and Petroleum Geology*, 2020, 117, pp.104382. 10.1016/j.marpetgeo.2020.104382 . hal-02892063

HAL Id: hal-02892063

<https://hal.sorbonne-universite.fr/hal-02892063v1>

Submitted on 7 Jul 2020

HAL is a multi-disciplinary open access archive for the deposit and dissemination of scientific research documents, whether they are published or not. The documents may come from teaching and research institutions in France or abroad, or from public or private research centers.

L'archive ouverte pluridisciplinaire **HAL**, est destinée au dépôt et à la diffusion de documents scientifiques de niveau recherche, publiés ou non, émanant des établissements d'enseignement et de recherche français ou étrangers, des laboratoires publics ou privés.

1 **Astronomical pacing of Late Cretaceous third- and second-order sea-level**
2 **sequences in the Foz do Amazonas Basin**

3
4
5 Slah Boulila^{1,2,*}, Célia Brange^{1,3}, Alberto Machado Cruz^{1,4}, Jacques Laskar², Christian Gorini¹, Tadeu
6 Dos Reis⁴, and Cleverson Guizan Silva⁵

7
8 * corresponding author

9
10
11 Email addresses: slah.boulila@sorbonne-universite.fr (S. Boulila), celia.brang@gmail.com (C. Brange),
12 albertomcruz88@gmail.com (A. Cruz), laskar@imcce.fr (J. Laskar), christian.gorini@sorbonne-universite.fr (C.
13 Gorini), tadeu.reis@gmail.com (T. Dos Reis), cguizan@id.uff.br (C. G. Silva).

14
15
16 ¹ Sorbonne Université, CNRS, Institut des Sciences de la Terre Paris, IStEP, F-75005 Paris, France

17 ² IMCCE, CNRS, Observatoire de Paris, PSL University, Sorbonne Université,
18 77 Avenue Denfert-Rochereau, 75014 Paris, France

19 ³ Institut Polytechnique UniLaSalle, 19 rue Pierre Waguët, B.P. 30313, 60026 Beauvais cedex, France

20 ⁴ Universidade do Estado do Rio de Janeiro, Faculdade de Oceanografia, Rua São Francisco Xavier,
21 524, 4º andar, sala 4028, Maracanã, 20550900 - Rio de Janeiro, RJ – Brasil

22 ⁵ Universidade Federal Fluminense, Departamento de Geologia, Av. Gen. Milton Tavares de Souza
23 s.n., Gragoatá – Niterói CEP: 24.210346

24
25
26 **Abstract**

27 Because of their relatively reduced tectonic influence, post-rift sedimentary
28 successions have a propensity to preserve climatically-driven cyclicity over long durations.
29 Here we present an integrated cyclostratigraphic and sequence stratigraphic study of the
30 post-rift Limoeiro sedimentary Formation (Fm) of the Foz do Amazonas Basin (offshore
31 Brazil), which spans the entire Late Cretaceous epoch (almost 35 Myr long). The principal
32 goal of the present study is to decipher very long (multi-Myr) sedimentary cyclicities and their
33 potential origin(s) in order to delineate the main controlling factors of post-rift sediment
34 sequences and packages.

35 We used gamma-ray (GR) well-log data for cyclostratigraphy, and seismic data for
36 sequence stratigraphy. Time-series analysis of GR data shows a rich series of Milankovitch
37 frequency bands. In particular, long-period cyclicities (405 kyr, 2.4 Myr, 4.7 Myr and 9.5 Myr)

38 are detected with high fidelity. Seismic and sequence stratigraphic interpretation shows a
39 striking sea-level (SL) depositional sequence order, matching the 4.7 Myr orbital cyclicity
40 inferred from cyclostratigraphy. Longer SL sequences interpreted in previous studies from
41 the Limoeiro Fm closely match the 9.5 Myr GR related orbital cycles.

42 Thus, we infer that the post-rift Limoeiro Fm was deposited continuously under
43 astronomical forcing over the Late Cretaceous epoch, resulting in an extraordinary record of
44 direct base- and sea-level responses to Milankovitch climatic forcing, including longer (multi-
45 Myr) periodicities. The 4.7 Myr orbital component is recorded for the first time in SL
46 sedimentary proxies, thus allowing here to update SL hierarchical orders. We suggest that
47 third-order, and second-order and suborders SL sequences were most likely paced by long-
48 period astronomical cycles (2.4 Myr eccentricity, and 4.7 and 9.5 Myr orbital cycles,
49 respectively.

50

51

52 **Keywords:** Cyclostratigraphy, sequence stratigraphy, climate, tectonics, Late Cretaceous,
53 Foz do Amazonas Basin.

54

55

56 1. Introduction

57 Climate and tectonics are the main competing factors in the sedimentary systems,
58 which together regulate base level in continents and sea level (SL) in oceans and seas.
59 While climate change controls SL depositional sequences at shorter timescales (few tens kyr
60 up to few Myr), in particular at Milankovitch cycle band (e.g., [Strasser et al., 1999](#); [Boullila et al., 2011](#)),
61 tectonic evolutions have been generally suggested to form SL depositional
62 sequences at longer timescales (Myr to few hundreds Myr) because major plate tectonic
63 motions occur at a very slow pace ([Vail et al., 1977](#); [Haq et al., 1987](#)). As such, global SL
64 (eustatic) sequences have been divided into different orders reflecting their amplitudes and
65 timescales as well as their controlling factors, i.e. climate or tectonics (e.g., [Vail et al., 1977](#);
66 [Haq et al., 1987, 1988](#); [Hardenbol et al., 1998](#); [Miller et al., 2005a](#); [Simmons, 2012](#)).

67 Precursor studies have shown the hierarchy of eustatic sequences from seismic data
68 and well-log stratigraphy ([Vail et al., 1977](#); [Haq et al., 1987, 1988](#)). In particular, [Vail et al. \(1977\)](#)
69 divided these eustatic sequences temporally into six orders ranging from tens
70 hundreds of millions years (first- and second-order) to tens of thousands years (sixth order).
71 First- and second-order SL sequences were ascribed to tectono-eustatic changes in the
72 global ocean volume, while fourth-, through sixth-order SL sequences were attributed to
73 climate change within the Milankovitch (insolation) band. However, third-order SL sequences
74 were interpreted as the result of climate or tectonic forcing ([Vail et al., 1991](#); [Cloetingh, 1988](#);

75 [Strasser et al., 2000](#)), while more recent studies have argued long-period (1.2 and 2.4 Myr)
76 Milankovitch forcing of Cenozoic and Mesozoic third-order SL cycles ([Boulila et al., 2011](#)). A
77 very recent study have proposed an updated SL sequence hierarchy and their potential
78 controlling factors, based on time-series analysis of the Phanerozoic reference eustatic data
79 ([Boulila et al., 2018a](#)).

80 Combined cyclostratigraphic and sequence stratigraphic studies increasingly show
81 that the role of climate and SL changes in the formation of depositional sequences is more
82 important, hence covering a wider frequency band ([Boulila et al., 2011; 2018a](#)). First
83 attempts made to relate third-order (and lower) eustatic sequences to long-period 1.2 and 2.4
84 Myr (and longer) Milankovitch cycles were based on a comparison of eustatic sequence
85 durations with orbital periodicities and/or on time-series analysis of compiled eustatic data
86 ([Boulila et al., 2011, 2018a](#)).

87 Another more effective approach is to perform an integrated cyclostratigraphic and
88 sequence stratigraphic study from a same sedimentary basin in order to decipher both SL
89 sequences and astronomical cycles for a potential link. Previous studies were hampered by
90 the lack of coupled climate and eustatic proxy data, or by the unavailability of very long
91 climatic proxy record susceptible to register multi-Myr climate and SL variations ([Boulila,](#)
92 [2019](#)).

93 Here we present an integrated cyclostratigraphic and sequence (seismic)
94 stratigraphic study on the Limoeiro sedimentary Formation (Fm) of the Foz do Amazonas
95 Basin (offshore Brazil), which spans the entire Late Cretaceous epoch (34.5 Myr long, from
96 66 to 100.5 Ma, [Gradstein et al., 2012](#)). The main objective of the present study is to seek
97 possible link between long-period (> 405 kyr) Milankovitch cycles inferred from
98 cyclostratigraphy and SL depositional sequences inferred from seismic stratigraphy.

99

100 **2. Geologic and stratigraphic settings**

101

102 **2.1. Geologic and stratigraphic setting of the Foz do Amazonas Basin**

103

104 The Amazon River Mouth Basin (also called "*Foz do Amazonas*" basin) is located in
105 the northwestern part of the Brazilian equatorial margin ([Fig. SI-1](#)). It covers an area of about
106 360000 km² ([Silva et al., 1999](#)). The Amazon Fan or Amazon Cone is situated in the center
107 of the basin. It is one of the largest river-fed mud-rich submarine fan systems in the world,
108 deposited over an area of 330000 km². It extends from the shelf break to 1100 km Northeast
109 offshore, up to about 4.8 km water depth ([Damuth et al., 1988](#)).

110 The Brazilian Equatorial Margin history began during the rifting and opening of the
111 Equatorial Atlantic Ocean, as a result of fragmentation and separation of northwestern

112 Gondwana (Fig. SI-2). According to Matos (2000), deformations associated with opening of
113 the South Equatorial Atlantic started as early as the Jurassic-Triassic (225-145 Ma), although
114 major rifting occurred too long later during late Barremian to late Albian (~120 to 105 Ma).
115 These deformations were mostly linked to transforming motion that generated a series of
116 complex marginal sedimentary basins, characterized by multiple phases of subsidence and
117 different structural styles (Figs. 1 and SI-3, Matos, 2000). The resulting transform fracture
118 zones correspond to structural lows as well as an area of deep grabens in the northwestern
119 part of the basin (Fig. 1). The Offshore Amazon basin, located in the westernmost part of the
120 the Equatorial Atlantic Ocean, is a particular basin of continental divergent passive margin
121 (e.g. Brandão and Feijó, 1994; Moulin et al., 2010)

122 The stratigraphic evolution of the Foz do Amazonas Basin depositional sequences
123 (Figs. 2 and 3). Two most recent publications providing the complete stratigraphy of the
124 basin come from Petrobras oil & gas Company (Brandão and Feijó, 1994; Figueiredo et al.,
125 2007). The pre-rift megasequence corresponds to the Calçoene Fm of Triassic-Jurassic age.
126 The syn-rift megasequence corresponds to the Cassiporé and Codó Fms, and spans the
127 Early Cretaceous epoch.

128 The post-rift megasequence encompasses the Limoeiro and Amapá Fms, spanning
129 together the Late Cretaceous through the Middle Miocene. The Limoeiro Fm, which is the
130 subject of the present study (detailed in Section 2.2), covers the Late Cretaceous epoch
131 (Figueiredo et al., 2007). It is overlaid by alternation of carbonates (Amapá Fm) and muddy
132 deltaic sediments (Marajó and Travosas Fms) deposited during the Late Paleocene through
133 the Middle Miocene. The present depositional system has started in the Late Miocene and
134 contributed to building the Amazon Fan, which is the most prominent feature in the basin,
135 called Pará Group's Stratigraphic Fms including Tucunaré, Piracuru and Orange Fms (Figs.
136 2 and 3).

137

138 **2.2. Stratigraphic framework of the studied Limoeiro Fm**

139 The Limoeiro Fm is a part of post-rift deposits, where its maximal thickness could
140 reach 2.5 km in depocenters and tilted grabens created during the rifting (Brandão and Feijó,
141 1994). In the present study, we have focused on data from the area of deep grabens, located
142 in the northwestern part of the basin (Figs. 1 and SI-3).

143 The transition between the Limoeiro Fm and the underlying Cassiporé Fm is marked
144 by an angular unconformity between the tilted syn-rift strata and the sub-horizontal post-rift
145 layers. The youngest post-rift layers are expressed in seismic data with moderate to strong
146 amplitude reflectors, continuous sub-horizontal, and gradually thickening towards offshore.
147 The upper boundary of the Limoeiro Fm was defined by the onset of the first carbonate
148 layers of the overlying Amapá carbonate platform Fm.

149 A potential source rock dated at around the Cenomanian-Turonian transition is about
150 500 to 1000 m thick below the Amazon fan (Cobbold et al., 2004), which was likely deposited
151 under anoxic marine conditions (Cobbold et al., 2004; Mello et al., 1989, 1995).

152 Because of intense basin gravity tectonics, especially in the central part of the basin,
153 Cenomanian-Holocene (100 Ma to present) deposits are affected by listric normal, thrust and
154 strike-slip faults (Cobbold et al., 2004; Perovano et al., 2009; Reis et al., 2010, 2016). Such
155 structural gravity-driven framework is rooted into three basal-detachment stratigraphic levels,
156 pointed out on seismic data (Silva et al., 1999; Cobbold et al., 2004; Perovano et al., 2009;
157 Reis et al., 2010, 2016): the older one, within the Limoeiro Fm dated at around 100 Ma,
158 accomodates an inherited thrust-and-belt system; a more important one, dated at about 65
159 Ma, acts as a regional basal detachment of modern and more complex thrust-and-belt
160 system, affecting both the carbonate platform and the Amazon-derived deposits; finally, the
161 younger and less important detachment, at around 10.5 Ma, locally affects the central
162 Amazon fan.

163

164

165 **3. Material and methods**

166

167 **3.1. Gamma-ray well-log data and seismic stratigraphy**

168 We used gamma-ray (GR) well-log data for cyclostratigraphy, and seismic data for
169 sequence stratigraphy. GR indicates the amount of radioactive atomic nuclei of uranium,
170 thorium, potassium, radium and radon in the rocks. GR has been successfully used as an
171 indirect paleoclimatic proxy to characterize orbitally driven continental and marine sediments
172 (e.g., Weedon et al., 2004; Wu et al., 2013). We have used GR data from the two wells APS-
173 29-AP and APS-44-AP (hereafter wells 29 and 44 respectively, Fig. 1), which covers the
174 whole Limoeiro Fm (Fig. 4). Resolution of GR data ranges from 15 to 20 cm, and their values
175 are expressed in API (American Petroleum Institute) unit. In wells 29 and 44, GR data range
176 from nearly 20 to 150 API, and the most important variations are mainly related to lithological
177 changes from clays, siltstones and sandstones (Fig. 4).

178 The seismic dataset includes approximately 20,000 km of 2D multi-channel seismic
179 data (made available by the Brazilian Navy and ANP-Brazilian Petroleum and Gas Agency)
180 and two blocks of 3D multi-channel seismic data covering 3,800 km² (made available by
181 CGG company).

182 Five 2D seismic lines useful for this study (Fig. SI-5) where only accessible as
183 pictures and without numerical data, so they were just useful for having a larger view outside
184 the 3D block, but they were not interpreted. The quality of these 2D multi-channel lines were
185 not good compared to the 3D multi-channel seismic block (Fig. SI-5). The northwestern 3D

186 seismic block (Fig. SI-5) also called BM-FZA-4/5 was acquired in 2007 by CGG. This PSTM
187 (Pre-Stack Time Migration) survey covers 1700 km² of 60 fold 3D data. This survey is a
188 medium good data knowing that the typical values of fold for modern 3D seismic data range
189 from 10 to 120. The minimal vertical resolution around the Limoeiro Fm depth is 40 m.

190 Well logs were integrated to seismic dataset based on standard tools for 1D depth-to-
191 travel time conversion available in Kingdom seismic interpretation software. Well 29 was tied
192 to the available seismic data using a synthetic seismogram generated with sonic log (DT),
193 density log (RHOB) and a seismic wavelet extracted from the seismic data (see
194 Supplementary Fig. SI-6). Well 44 was tied to the available seismic data using check-shot
195 data acquired in the well's drilling site (approximately one travel-time measurement every 60
196 measured meters).

197

198 **3.2. Bio-lithostratigraphy and total organic carbon (TOC) data**

199 The Limoeiro Fm in wells 29 and 44 was entirely recovered by the wireline log. The
200 base of the formation corresponds to an angular unconformity between the syn-rift and post-
201 rift deposits. Additional analyses to check this boundary were made using the seismic data.
202 The top of the formation is the sharp contact with the overlying carbonate deposits.

203 The Limoeiro Fm is 800 m thick in Well 29, and 1476 m thick in Well 44. This
204 difference in thickness is due to the more proximal position of Well 44 with respect to Well
205 29. The lithology in Well 29 is dominated by claystones and siltstones, while Well 44 is
206 predominantly composed of claystones and sandstones (Fig. 4).

207 The Limoeiro Fm was assigned to the entire Late Cretaceous epoch (Figueiredo et
208 al., 2007). However, the only available biostratigraphic data provide constraints on the age of
209 its upper boundary, acquired from Well 1-APS-45B-AP (hereafter Well 45B, Fig. SI-7). This
210 well was drilled down to the Maastrichtian, where a calcareous nannofossil biomarker (*Micula*
211 *murus*) was found around the top of the Limoeiro Fm. Its first and last occurrences were
212 detected around 20 meters before the end of Well 45B (Fig. SI-7), thus providing ages of
213 approximately ~69 and ~66 Ma (Burnett 1998; Lees and Bown, 2005). The ~66 Ma age
214 corresponds most likely to the top of the Limoeiro Fm (Fig. SI-7). Consequently, only the top
215 of the Limoeiro Fm is relatively well dated by biostratigraphy.

216 Several geochemical data were acquired, but with low resolution. We have focused in
217 this study on the Total Organic Carbon (TOC) data to potentially detect organic-rich
218 stratigraphic levels associated with the Oceanic Anoxic Event 2 (OAE2, 'Bonarelli Level') of
219 the Cenomanian-Turonian transition (e.g., Mello et al., 1989), and eventually the OAE1d
220 ('Breistroffer Level') of the latest Albian. The 'Bonarelli' OAE2 has been documented
221 worldwide (e.g., Schlanger and Jenkyns, 1976; Paul et al., 1999; Tsikos et al., 2004;
222 Jenkyns, 2010; Jarvis et al., 2011). Also, the Breistroffer OAE1d has been recorded in

223 several basins including the Atlantic and Pacific oceans ([Wilson and Norris, 2001](#); [Navarro-](#)
224 [Ramirez et al., 2015](#)).

225 Only Well 29 exhibits TOC data ([Fig. 4](#)), but with a variable sampling step, which
226 ranges from 3 to 30 m. TOC data vary from 0.3 to 4.4 % with two distinguishable intervals of
227 higher TOC values (> 3 %), one at around 4320 m depth and the other at around 4470 m
228 depth. Interestingly, the sampling step at these two intervals is the smallest, thus providing
229 the highest resolution of 3 m. We have explored these two intervals as potential records of
230 OAE2 (e.g., [Mello et al., 1989](#)) and OAE1d ([Section 5.2](#)).

231

232 **3.3. Methods**

233

234 **3.3.1. Time-series analysis**

235 We used the multi-taper method (MTM) spectral analysis ([Thomson, 1982](#)) to detect
236 sedimentary cyclicities in GR data. MTM spectra were conducted using three 2π tapers,
237 together with the robust red noise test ([Mann and Lees, 1996](#)) as implemented in the R
238 package ‘astrochron’ freeware ([Meyers, 2014](#)). Prior to spectral analysis, GR data were
239 detrended using the weighted-average lowess method ([Cleveland, 1979](#)). We also used the
240 gaussian filter ([Paillard et al., 1996](#)) to extract the recorded astronomical cycles.

241 Astronomical time calibration (or tuning) of the Mesozoic records is problematic
242 because of the lack of accurate orbital solutions that can be used for tuning stratigraphy older
243 than about 50–60 Ma ([Laskar et al., 2004, 2011](#)). Fortunately, there is one notable exception:
244 the 405 kyr orbital eccentricity term, which can be estimated with high accuracy throughout
245 the Mesozoic Era ([Laskar et al., 2004](#)).

246 As the analyzed interval (i.e., the Limoeiro Fm) covers approximately 35 Myr of Late
247 Cretaceous, dramatic changes in the sedimentation rate have been observed. Additionally,
248 lithostratigraphy of the two wells sometimes shows intervals with homogeneous lithology,
249 and sometimes intervals with pronounced lithological changes ([Fig. 4](#)). For instance, the
250 more proximal Well 44 shows, from the base of the Limoeiro Fm till depth ~3200 m, quasi-
251 homogeneous lithology dominated by clays. However, the upper part of the Limoeiro Fm in
252 Well 44 exhibits prominent alternations of clayey and sandy lithologies. Such differences in
253 the lithology along each well strongly affects GR variations, with the more homogeneous
254 intervals being characterized by lower amplitudes and intervals with contrasted lithologies by
255 stronger amplitudes ([Fig. 4](#)).

256 To reduce the impact of the aforementioned factors on GR variations, i.e. the lithology
257 and changes in sedimentation rate, we have conducted a cyclostratigraphic analysis per
258 intervals in each well. The length of the selected intervals is not constant between the two
259 wells and even within each well. It depends on the lithological change, and on the

260 wavelengths of high- and low-frequency cyclicities. Our approach was first to analyze short
261 intervals to capture precession, obliquity and short eccentricity cycles, then analyze longer
262 intervals to capture several 405 kyr eccentricity oscillations ([Supplementary Information SII](#)).
263 We used frequency ratio method to infer to the statistically detected sedimentary cycles a
264 Milankovitch astronomical origin ([Section 4.1](#)).

265 Finally, we focused on the wavelength related to the 405 kyr eccentricity component.
266 We bandpass filtered it, tuned each analyzed interval to a pure 405 kyr periodic signal
267 ([Laskar et al. 2004](#)), and assembled all the 405 kyr tuned intervals in order to merge and
268 define an age model for each well, called floating timescale (e.g., [Hinnov and Hilgen, 2012](#)).
269 The obtained 405 kyr floating timescale was then anchored to the age of onset of OAE2
270 (94.17 Ma, [Batenburg et al., 2016](#)), which corresponds to a maximum of a 405 kyr
271 eccentricity cycle in La2011 astronomical model ([Laskar et al., 2011](#)). Finally, the 405 kyr GR
272 cycle extremes were tied to the 405 kyr La2011 eccentricity cycles in order to obtain an
273 absolute astronomical timescale.

274 We applied spectral analysis to the whole (405 kyr) GR calibrated Limoeiro Fm to
275 seek very long-period Milankovitch cycles. In particular, the output 405 kyr tuned GR series
276 could be examined for alignment of other, higher frequency terms associated with for e.g.,
277 the short (100 kyr) eccentricity, the lower frequency terms associated with g1-g5, s4-s3, g4-
278 g3 (0.95, 1.2 and 2.4 Myr Cenozoic mean periods, [see Table 1](#)), with a special focus on the
279 very longer orbital periods of 4.7 and 9 Myr ([Boullila et al., 2012](#); [Boullila, 2019](#)). These longer
280 periods will be potentially compared to SL depositional sequences inferred from seismic
281 data.

282

283 **3.3.2. Sequence and seismic stratigraphy**

284 Well 29 presents a reference record in the Foz do Amazonas Basin, which was used
285 to describe the sequence stratigraphic framework of the Limoeiro Fm ([Fig. 2](#)). Wells 29 and
286 44 are the only ones connected with seismic data, thus having the potential to realize a direct
287 correlation between SL sequences inferred from seismic data and astroclimatic cycles
288 inferred from GR data. In order to characterize the main horizons and identify major
289 unconformities and sequence boundaries, the seismic interpretation was based on the
290 analysis of seismic stratigraphic terminations. Their organization is related to the acoustic
291 impedance contrast between genetically related strata, leading to the identification of
292 sedimentary bodies within a stratigraphic sequence. We have used the Kingdom software,
293 which is dedicated to correlate the main horizons across the northwestern 3D block between
294 Well 44 (north of the block) and Well 29 (south of the block). On the overall progradation of
295 the Limoeiro seismic megasequence, major unconformities have been identified based on
296 the classical seismic stratigraphy (e.g., [Vail et al., 1977](#); [Haq et al., 1987, 1988](#); [Christie-Blick](#)

297 et al., 1990; Miller et al., 2018; Catuneanu, 2019). The recognition of major stratigraphic
298 surfaces on the seismic data is based on stratigraphic principles as defined by Vail et al.
299 (1977), with mainly Maximum Flooding Surfaces (MFS) characterized by downlap surfaces
300 and Sequence Boundaries (SB) identified by both onlap and truncation or erosional surfaces.
301 Projection of MFS and SB into borehole logs were performed using synthetic seismograms
302 (created using check shots and sonic and density logs, see [Supplementary Fig. SI-6](#)).

303

304

305 **4. Results**

306

307 **4.1. Cyclostratigraphy**

308 Power spectra of the Limoeiro Fm in depth domain in Well 29 shows two strong
309 peaks of 240 and 56 m ([Fig. 5A](#)). Power spectra per intervals highlight additional peaks, in
310 particular two peak bands in the order of 10 and 2.5 m ([Fig. SII-1](#); [Fig. 5A](#)). Frequency ratio
311 method indicates short (100 kyr), 405 kyr (g2-g5), and 2.4 Myr g4-g3) eccentricity periods for
312 respectively peaks 2.5, 10 and 56 m. Power spectra in the 405 kyr time domain (see
313 [Methods](#)) calibrates the 240 m peak to a period of 9.7 Myr, the 56 m peak to a period of 2.4
314 Myr, the peaks around 2.5 m to periods around 100 kyr ([Fig. 5B](#)), thus reciprocally matching
315 the eccentricity components. Two other peaks of 30 and 23 m are calibrated to 1.3 and 1.0
316 Myr respectively, thus they may correspond to s4-s3 and g1-g5 orbital frequencies ([Table 1](#)).

317 Power spectra of the Limoeiro Fm in Well 44 shows two strong peaks of 383 and 203
318 m ([Fig. 5C](#)). Power spectra per intervals highlight several additional peaks of wavelengths of
319 96, 50, 17, 7.5 and 4 m ([Fig. SII-2](#); [Fig. 5C](#)). Frequency ratio method conjointly with the g2-g5
320 orbital tuning indicates that the shortest 4 m wavelength may correspond to the short
321 eccentricity, the 7.5 m to s3-s6 (173 kyr, see [Boullila et al., 2018b](#)), the 17 m to g2-g5 (405
322 kyr target), the 50 m to s4-s3 (1.2 Myr), the 96 m to g4-g3 (2.4 Myr), and the 203 and 383 m
323 to 4.7 and 9.5 Myr orbital periods respectively (see also [Table 1](#)).

324 The 405 kyr (g2-g5) tuning in the two wells ([Figs. 6 and 7](#)) yields the same duration of
325 ~35 Myr (equivalent to eighty six g2-g5 cycles) for the Limoeiro Fm ([Fig. 8](#)). Evaluation of
326 orbital age models is discussed in [Section 4.2](#).

327 The recorded orbital cycles in GR data sometimes match the lithology, but sometimes
328 they do not. For instance, in apparently homogeneous claystone or sandstone intervals,
329 significant orbitally controlled GR fluctuations could be observed ([Figs. 6 and 7](#)). Also, there
330 is no preferentially expressed orbital parameter within the lithology. Dominant cyclic
331 (alternating) lithologies could sometimes match the short eccentricity, and sometimes the
332 long 405 kyr eccentricity ([Fig. SII-2](#)).

333

334 4.2. Sequence and seismic stratigraphy

335 The top and the base of the Limoeiro Fm are marked by reflectors with high
336 amplitude, which can be followed from north to south of the 3D seismic block.

337 Seismic Inline 3273 crosses exactly at the level of Well 29. With the maximal vertical
338 resolution of 40 m, Inline 3273 shows 20 reflectors within the Limoeiro Fm equivalent
339 interval, but these reflectors could not be extrapolated neither till Well 29 site nor till Well 44
340 site along the crosslines or the arbitrary lines.

341 The log and seismic calibration was derived from inline 1454, which was tied to Well
342 44 located in the northern part of the 3D seismic block. Seismic resolution is not very good
343 (about 40 m); however, the studied interval is thick enough (1476 m thick in Well 44) to
344 identify the major depositional sequences. Picking is based on stratigraphic principles, with
345 mainly MFS characterized by downlap surfaces, and SB by both onlap and truncation or
346 erosional surfaces. Taking into account the location of Well 44, which is relatively proximal,
347 we found mainly systems tracts related to transgressive and regressive phases (Figs. 9 and
348 10). However, when moving seaward we can observe on the seismic data the development
349 of main lowstand systems tracts (LST) which are rooted on the main sequence boundaries.
350 As a result, we picked seven MFS and six SB. Thus, six well-defined sequences in Well 44
351 (interval from about 2200 m till about 3250 m) were the subject of a potential correlation with
352 long-period astroclimatic cycles inferred from GR data.

353 The identification of LST is based on the position of marine onlaps on the paleoslopes
354 (LST in orange-shaded areas in Fig. 9). The erosional unconformities (red lines in Fig. 9,
355 subareal unconformities on paleoplatforms *sensu* Catuneanu, 2006), with their correlative
356 conformities basinward, were placed at the base of the identified LST. They have been
357 interpreted as major SB *sensu* Posamentier and Vail (1988). Back step geometries
358 characterize the transgressive intervals (thickening toward the continent). The green
359 surfaces on top of these intervals are materializing the downlap surfaces. More generally,
360 these green surfaces correspond to the turning point between retrogradation (back step
361 geometries on the seismic data, with a thickening toward the continent) to the progradation
362 (downlaps), and correspond to maximum floodings.

363 All seismic units above Sequences boundaries (SB, *sensu* Vail et al., 1977) show
364 poorly stratified series basinward, indicating that unstable shelf edges led to mass wasting of
365 unconsolidated sediments. Some of the shelf edges also show listric detachments (see Fig.
366 9). Consequently, the shelf edge presents chaotic internal geometries, indicating that these
367 collapses originated mass transport deposits (MTDs) to the deeper basin. Abrupt
368 terminations of the topset beds, indicate that mass movement of material to the deeper basin
369 has been completed prior to subsequent flooding. Discussion about the nature of LST is
370 beyond the scope of this paper, however, we infer that mass-transport processes described

371 for Quaternary strata by several authors (e.g., [Damuth and Kumar, 1975](#); [Damuth and](#)
372 [Embley, 1981](#); [Maslin et al., 1998](#)), and for older Pliocene sediments (see also [Reis et al.,](#)
373 [2010](#); [Silva et al., 2010](#); [Gorini et al 2013](#)) may have been also operative since the early
374 post-rift evolution of the margin and could be part of the lowstand deposits.

375

376 **5. Discussion**

377

378 **5.1. Evaluation of g2-g5 orbital age models**

379 The Limoeiro Fm was poorly dated in the literature. It was roughly attributed to the
380 entire Late Cretaceous epoch ([Figueiredo et al., 2007](#)) with only one chronostratigraphic age
381 control (~66 Ma) at its upper boundary, inferred from calcareous nannofossil biostratigraphy
382 ([Section 3.2](#)).

383 The absolute g2-g5 age model in Well 29 depends on the anchoring age point at the
384 onset of OAE2 (94.17 Ma, [Batenburg et al., 2016](#)) assuming that the start of TOC peak, at
385 4320 m depth, records the onset of this event. Such age model provides an age of 66.472
386 Ma for the top of Limoeiro Fm ([Fig. 6](#)). This age is older than the biostratigraphically inferred
387 age of ~66 Ma, by only one g2-g5 equivalent cycle. In addition, the g2-g5 age model in Well
388 29 yields an age of 100.35 Ma for the lower TOC peak (4470 m depth) that we suspect to
389 document the OAE1d ([Section 3.2](#)). The duration between the starts of the two TOC peaks
390 assumed to record the OAE2 and OAE1d is 6.180 Myr (from 100.35 to 94.17 Ma), which is
391 close to that reported in the literature (e.g., ~6 Myr, [Sprovieri et al., 2013](#)).

392 Well 44 provides additional constraints on g2-g5 age model. Interestingly, the
393 Limoeiro Fm encompasses the same number of g2-g5 cycles in the two wells (i.e., 86 cycles,
394 [Figs. 7 and 8](#)). Because of the absence of TOC data in Well 44, g2-g5 floating timescale in
395 this well was anchored at the base of a GR peak (3650 m depth), which is correlatable to a
396 GR peak in Well 29, assumed to match the OAE1d (100.35 Ma in Well 29). The resulting
397 absolute g2-g5 age model in Well 44 provides an age of 66.646 Ma for the top of the
398 Limoeiro Fm, which is only 0.174 Myr older than the 66.472 Ma astronomical age in Well 29.
399 Furthermore, the base of a very strong, well-defined GR peak within a clayey interval in Well
400 44 (at 3395 m depth) has surprisingly an age of 94.10 Ma. We suspect that this strong peak
401 in Well 44 may match the equivalent OAE2 interval in Well 29 ([Fig. 8](#)).

402 In summary, three remarkable age points from g2-g5 age model in Well 29, which is a
403 reference well in the Foz do Amazonas Basin (see above), could be considered in future
404 studies are: (1) the top of the Limoeiro Fm at ~66.472 Ma, (2) the start of the older TOC peak
405 at ~100.35 Ma matching the OAE1d and nearly the base of the Limoeiro Fm, and (3) the
406 start of the younger TOC peak at ~94.17 Ma, corresponding to the onset of OAE2.

407 Although the consistency in age models between the cyclostratigraphically calibrated
408 wells 29 and 44 and previous studies of the Limoeiro Fm (e.g., [Figueiredo et al., 2007](#)), the
409 only available biostratigraphic age of the upper limit of the Limoeiro Fm ([Supplementary Fig.
410 SI-7](#)) may weaken the potential of g2-g5 age models for use in future studies.
411 Biostratigraphic age control is of paramount importance in the generation of astronomical
412 timescales (ATS), because it is an independent approach on which the ATS should be built
413 (e.g., [Hinnov and Hilgen, 2012](#)). However, in the absence of accurate ages from
414 biostratigraphy (or integrated biochronostratigraphy), g2-g5 orbital tuning has been used with
415 success for Mesozoic and Cenozoic cyclostratigraphy (e.g., [Boulila et al., 2008, 2010](#);
416 [Hinnov and Hilgen, 2012](#) ; [Liu et al., 2018](#)). The identification of 405 kyr (g2-g5) eccentricity
417 cycle could be successfully fulfilled using frequency ratio method (e.g., [Huang et al., 1992](#);
418 [Mayer and Appel, 1999](#); [Boulila et al., 2008](#) their table 1; [Hinnov and Hilgen, 2012](#)). Tuning
419 wells 29 and 44 to a pure 405 kyr periodicity ([Laskar et al., 2011](#)) allows to correct
420 considerable variations in sedimentation rates, and the alignment of other, higher and lower
421 frequency terms ([Section 4.1](#)). Thickness of the 405 kyr related eccentricity cycles ranges
422 from 7 to 11.8 m in Well 29, and from 8.7 to 24.5 m in Well 44 ([Section 4.1](#) and
423 [Supplementary information II](#)). The g2-g5 age models calibrate wavelengths to temporal
424 periods, which are very close to those predicted in the astronomical models. In particular,
425 shorter wavelengths related to the short eccentricity cycles are calibrated to periods around
426 100 kyr ([Figs. 5B,D](#)). The longer wavelengths, related to g4-g3 eccentricity component, are
427 calibrated to a period of 2.4 Myr ([Fig. 5B](#)). Thus, the 405 kyr tuning further supports
428 cyclostratigraphic interpretations inferred from frequency ratio method ([Section 4.1](#)).
429 Accordingly, we used the potential of g2-g5 age models to explore long-period cyclicities and
430 their possible impact on SL changes.

431

432

433 **5.2. Astronomical origin of the 4.7 Myr cycles**

434 The strong expression of the 4.7 Myr orbital cyclicity in SL record leads us to discuss
435 its possible origin in more detail. A ~4.7 Myr cyclicity can be directly retrieved in the
436 eccentricity time series as the libration period of the resonant argument $\theta = 2(g_4 - g_3) - (s_4$
437 $- s_3)$, where g3, g4 are related to the precession of the perihelions of the Earth and Mars,
438 and s3, s4 are related to the precession of the nodes of the same planets ([Laskar, 1990](#)). It
439 could also be retrieved from the obliquity time series ([Supplementary information III](#)). More
440 precisely, it could be obtained when one considers only the proper modes of the secular
441 frequencies in the precession of perihelia and nodes of the inner planets ([Fig. SIII-1](#)). The
442 ~2.4 and ~4.7 Myr are present either in the precession of perihelia or in the precession of

443 nodes, but with different phase relationships. They are in phase at the ~4.7 Myr band, but
444 antiphased at the ~2.4 Myr band (Fig. SIII-1).

445 In fact, Laskar (1990) highlighted a fundamental libration period of ~4.7 Myr
446 for θ (so-called here as P_θ and the correspondent frequency as F_θ). This libration oscillation
447 corresponds to the oscillations of a pendulum, which is close to what occurs in case of
448 resonances, when a combination of frequencies becomes null (here $2(g_4 - g_3) - (s_4 - s_3) =$
449 0). The four frequencies g_3, g_4, s_3, s_4 are no longer independent and a new frequency, the
450 libration frequency, appears as a new independent frequency ($F_\theta = 0.28$ arcsec/yr, $P_\theta \approx 4.7$
451 Myr). Here, the frequency of libration F_θ is itself in rational ratio with ' $g_4 - g_3$ ' ($2F_\theta = g_4 - g_3$
452 $= 0.58$ arcsec/yr ≈ 2.4 Myr) as was observed in Laskar (1990). Amplitude harmonic analysis
453 of variations of the resonant argument θ (Fig. 11) shows a strongest peak at ~4.7 Myr, which
454 represents the fundamental libration frequency F_θ . Then, harmonics of F_θ (i.e., $2F_\theta, 3F_\theta, 4F_\theta,$
455 $5F_\theta, 6F_\theta, 7F_\theta$) appear in the spectrum, with a dominance of odd mode resonance
456 frequencies ($3F_\theta, 5F_\theta, 7F_\theta$). A ~1.6 Myr period appears that can be related to a combination
457 of F_θ , i.e., $3F_\theta$ (0.84 arcsec/yr ≈ 1.6 Myr). This periodicity, which also modulates the climatic
458 precession at the two terms ' $p+g_4$ ' and ' $p+g_3 - F_\theta$ ' (Table 1), was recently detected in the
459 Cenozoic climatic record (Bouilila, 2019). The ~4.7 Myr cyclicity in the eccentricity time series
460 is also modulating the climatic precession at the two frequencies ' $p+g_3$ ' and ' $p+g_3 + F_\theta$ '
461 (Table 1). Such long-term cyclicity has been detected in the sedimentary carbon-cycle
462 proxies (Bouilila et al., 2012; Spovieri et al., 2013), and may have an impact on SL change
463 (Section 4.3).

464

465 5.3. Third- and second-order SL sequences: durations and causal mechanisms

466 Precursor studies have considered the important role of sea-level changes in the
467 sedimentary records, and thus proposed an hierarchical link among different orders of SL
468 depositional sequences (e.g., Vail et al., 1977; Haq et al., 1987, 1988). This hierarchical link
469 is based on magnitude and duration of SL sequences. While the quantification of magnitude
470 (or amplitude) of SL fluctuations has received controversial interpretations (Vail et al., 1977;
471 Haq et al., 1987; Miller et al., 2005; Kominz et al., 2008; Müller et al., 2008), assesment of
472 timing and duration of SL sequences has generally been agreeable among researchers (e.g.,
473 Haq et al., 1987; Miller et al., 2005). Although amplitude of SL oscillations is a fundamental
474 criterion for sequence order determination (e.g., Vail et al., 1977), studies based on timing
475 and duration of Mesozoic-Cenozoic SL sequences yield strong correlation between third-
476 order SL sequences and long-period orbital cycles (Bouilila et al., 2011).

477 Here we focus on durations of both third- and second-order SL sequences and their
478 potential link with long-period astronomical cycles. Integrated cyclostratigraphic and
479 sequence stratigraphic study of the Limoeiro Fm hints at a connection between orbital forcing

480 and SL change at these two orders (Sections 4.1 and 4.2). Seismically mapped depositional
481 sequences have been considered to reflect SL fluctuations (e.g., Vail et al., 1977; Haq et al.,
482 1987, 1988; Christie-Blick et al., 1990; Miller et al., 2018; Catuneanu, 2019). In particular,
483 prominent SL sequences, detected seismically in the Limoeiro Fm, closely match the 4.7 Myr
484 orbital cycles inferred from GR cyclostratigraphy (Figs. 9 and 10). Longer SL sequences
485 were previously interpreted in the Limoeiro Fm (Brandão and Feijó, 1994; Figueiredo et al.,
486 2007), and these sequences closely match the 9.5 Myr orbital cycles inferred from GR
487 cyclostratigraphy (Fig. 10).

488 The 9.5 Myr cycles were attributed to shorter second-suborder SL sequences (Haq et
489 al., 1987; discussed in Boulila et al., 2018a). However, the 4.7 Myr orbital cycle band has
490 never been discussed in depth in SL proxies. It was evoked in Toarcian SL sequences
491 (Boulila et al., 2014 their figure S6), but discussed in more detail in Cenozoic carbon-cycle
492 data (Boulila et al., 2012, see their figures S2 and S4), and more recently in temperature
493 proxy data (benthic $\delta^{18}\text{O}$) (Boulila, 2019). The 4.7 Myr orbital cyclicity is prominent in SL
494 record (Section 4.2), thus it is used to update SL sequence hierarchy (Table 2).

495 Third-order sequences match 1.2 Myr (s4-s3) obliquity in icehouses and 2.4 Myr (g4-
496 g3) eccentricity in greenhouses, while fourth-order sequences were interpreted to reflect
497 kyr eccentricity cycle (Boulila et al., 2011, 2014). Neither the 2.4 Myr (third-order) nor the 405
498 kyr (fourth-order, Boulila et al., 2011) eccentricity cycles are seismically captured in this
499 study, likely because of low resolution of seismic data. However, high-resolution
500 cyclostratigraphic study shows evidence for a strong expression of 405 kyr and 2.4 Myr
501 eccentricity in the Late Cretaceous greenhouse (Fig. SII-3), which most likely correspond to
502 fourth- and third-order SL sequences, respectively.

503 In a recent study (Boulila et al., 2018a), SL orders and suborders were updated on
504 the basis of time-series analysis of the Phanerozoic SL data. Indeed, second-order SL
505 sequences have two suborders: 9.5 and 36 Myr (Boulila et al., 2018a). Here we add to them
506 another suborder, which corresponds to 4.7 Myr orbital band (Table 2). Thus, second-order
507 SL sequences possesses now three suborders: the shortest is the 4.7 Myr band, the middle
508 one corresponds to the 9.5 Myr band, and the longest one match the 36 Myr cycle band. The
509 4.7 and 9.5 Myr SL cyclicities have most likely a Milankovitch astronomical origin (Section
510 4.2; Boulila et al., 2012). The 36 Myr SL cycle has been ascribed to another dimension of
511 astronomical forcing (vertical motion of the solar system) and/or to tectonics (Boulila et al.,
512 2018a) (Section 5.4). It is worthwhile that another 16-18 Myr cycle band, hence falling into
513 the second-order timescales (Table 2), could be barely seen in the analyzed GR records,
514 because the signals are too short to determine its actual period. There are potentially two 16-
515 18 Myr oscillations (Fig. 10). Nevertheless, such cyclicity could be retrieved from compiled
516 SL data of the past 110 Ma (Fig. SIV-1) (see also figure 2 of Boulila, 2019).

517 The hierarchical link between durations of third-order, and second-order and
518 suborders SL sequences (1.2, 2.4, 4.7, 9.5, 18, 36 Myr) leads us to reassess the role of
519 astronomical forcing in the formation of SL depositional sequences. Although such link hints
520 at a connection between SL and astronomically driven climates, global tectonic forcing on SL
521 change, at 9.5 Myr band and longer, could not be excluded ([Section 5.4](#)).

522 Even at shorter timescales, tectonics undoubtedly interferes within the sedimentary
523 SL archive. However, the principal cause that emerges in the SL record at the million to
524 multi-million year timescale is seemingly the astro-climatically driven signal.

525

526 **5.4. Tectonic versus climate control of sea-level changes**

527 Eustasy or global mean sea-level (e.g., [Haq et al., 1987](#); [Myers and Milton, 1996](#);
528 [Miller et al., 2018](#)) has received a particular interest in several geoscience domains because
529 of its numerous potential implications for petroleum exploration, biogeochemical cycles,
530 biomass evolutions and turnovers, and the development of the geological time scales (see
531 [Simmons, 2012](#); [Simmons et al., in press](#) for extensive reviews). Thus, the study of eustatic
532 drivers is of paramount importance to better understanding the related geological processes.
533 In particular, assessment of the duration of eustatic sequences can help to decipher their
534 causal mechanisms ([Table 2](#)).

535 Although long-term (100 to several 100s of Myr) eustatic variations have generally
536 been seen as the result of changes in the global ocean volume induced by plate tectonic
537 motions, outstanding questions remain on the cause of shorter term eustatic changes of few
538 Myr to several 10s of Myr.

539 For instance, paleo-tectonic reconstructions show a correlation between major
540 tectonic phases and eustatic sequences at the Wilson-Cycle scale, of duration of 250-300
541 Myr ([Cogné et al., 2006](#)). However, the pronounced 36 Myr eustatic cyclicity observed
542 throughout the Phanerozoic eon has not found its equivalent in the tectonic variations,
543 possibly because the absence of accurate paleo-tectonic reconstructions ([Boullila et al.,](#)
544 [2018](#)). Thus, another alternative cause from the vertical motion of the solar system in the
545 galaxy via the incident cosmic rays has been equally suggested, though the impact of cosmic
546 rays on climate is a debated subject ([Table 2](#)).

547 Milankovitch orbital forcing of insolation driven climate has been widely argued ([Hays](#)
548 [et al., 1976](#); [Hinnov, 2015](#); [Hilgen, 2010](#)), and today there are increasing evidences for
549 Milankovitch control of climate, carbon-cycle and sea-level at Myr to multi-Myr timescales
550 ([Boullila et al., 2011](#) and references therein; [Boullila et al., 2012](#); [Sprovieri et al., 2013](#); [Boullila,](#)
551 [2019](#)).

552 The 1.2 Myr obliquity and 2.4 Myr eccentricity cycles have been recognized in both
553 the astronomical and geological variations (e.g., [Laskar et al., 2004](#); [Pälike et al., 2004](#),

554 [2006](#)), and their impacts on sea-level sequences have been argued (see [Boulila et al., 2011](#)
555 for an extended review). The 4.7 Myr orbital cyclicity has less been identified in the
556 astronomical and geological variations ([Boulila et al., 2012, 2014](#); [Sprovieri et al., 2013](#);
557 [Boulila, 2019](#)). The 4.7 Myr has been detected in both the eccentricity and obliquity signals
558 ([Boulila et al., 2012](#)) (see [Section 5.2](#) for its precise origin). The 9.5 Myr orbital cycle has
559 been retrieved for the first time from the modulation of both the eccentricity and obliquity
560 signals ([Boulila et al., 2012](#); [Boulila, 2019](#)). Its record in the geological archives has been
561 successfully retrieved from deep-sea (benthic foraminifera) stable carbon and oxygen
562 isotopes ([Boulila et al., 2012](#); [Boulila, 2019](#)).

563 At ten to tens of Myr timescales, geodynamic modeling has shown different cyclicities
564 of ~25 Myr for the spreading and production rates of oceanic ridges ([Cogné and Humler,](#)
565 [2006](#)), and of 25-50 Myr and 10-15 Myr for arc magmatism ([DeCelles et al., 2009](#); [Wolfram](#)
566 [et al., 2019](#)), although some studies have pointed to the fractal nature of arc magmatism
567 (e.g., [de Silva et al., 2015](#)). Interestingly, extended synthetic observations throughout the
568 Phanerozoic eon from the Canadian High Arctic show 10 Myr pseudo-periodic sedimentary
569 sequences correlated to tectonic episodes ([Embry et al., 2019](#)). Such study indicates that
570 tectonics from uplift and subsidence was responsible for the formation of depositional
571 sequences of durations ranging from 4 to 17 Myr. These durations overlap with the 4.7 and
572 9.5 Myr orbital cycles, leading us to reassess the importance of a coupled climate and
573 tectonics effect that could play a role in SL changes at ten to tens of Myr timescales.
574 Intriguing match between variations in external (climate) and Earth's interior processes has
575 been observed at shorter ([Kutterolf et al., 2012](#); [Crowley et al., 2015](#); [Huybers and Langmuir,](#)
576 [2009](#)) and longer ([Boulila, 2019](#)) timescales, pointing to potential feedback responses of
577 Earth's interior dynamics to astronomically driven climate and Earth's surface processes (see
578 also discussion in [Boulila, 2019](#)). For instance, orbitally paced glacial cycles have been
579 correlated to oceanic crust production ([Crowley et al., 2015](#)).

580

581 **5.5. Sea-level drivers in the Late Cretaceous "greenhouse"**

582 The Late Cretaceous represents one of the warmest epochs of the past 150 Ma, with
583 extreme greenhouse conditions culminating at the Cenomanian-Turonian Transition (e.g.,
584 [Friedrich et al., 2012](#); [Huber et al., 2018](#)). Because there is no direct sedimentary evidence
585 for polar ice caps, Earth has long been considered as ice free during the Late Cretaceous, in
586 addition to the highest sea levels (SL) that this epoch documents (e.g., [Haq et al., 1987](#); [Haq,](#)
587 [2014](#); [Miller et al., 2005a](#)).

588 Despite the extreme warmth and highest SL conditions, Earth's climate witnessed
589 severe, short-lived cooling events, coeval to prominent SL drops ([Haq and Huber, 2016](#);
590 [Galeotti et al., 2009](#)). These climatic coolings and SL falls have been argued worldwide on

591 the basis of stable oxygen isotopes and sedimentological proxy data (e.g., [Haq et al., 1987](#);
592 [Stoll and Schrag, 2000](#); [Bornemann et al., 2008](#)). Nevertheless, the record of prominent SL
593 fluctuations (ca. 20 to 110 m, e.g., [Haq, 2014](#)) during the so-called ice-free Late Cretaceous
594 epoch has generated an outstanding debate since the 1980's, regarding the existence (or
595 not) of ice sheets on Earth, that may explain these rapid sea-level falls via glacio-eustasy
596 (e.g., [Matthews, 1984](#); [Stoll and Schrag, 1996, 2000](#); [Huber et al., 2002](#); [Miller et al., 2005b](#);
597 [Bornemann et al., 2008](#); [Boullila et al., 2011](#); [MacLeod et al., 2013](#), among others).

598 Other causal mechanisms of short-term (e.g., Myr to multi-Myr) SL changes during
599 the Cretaceous have been suggested on the basis of changes in the aquifer water volume
600 and groundwater storages, i.e. aquifer-eustasy ([Jacobs and Sahagian, 1993](#)) or thermal
601 expansion and contraction of seawater column i.e., thermo-eustasy ([Gornitz et al., 1992](#);
602 [Schulz and Schäfer-Neth, 1998](#)). However, such mechanisms could generate only few to
603 tens of meters of SL oscillation (not more than 40 m). The aquifer-eustasy hypothesis has
604 been recently resumed to explain Cretaceous SL changes ([Wendler et al., 2016](#); [Wagreich et
605 al., 2014](#); [Sames et al., 2016](#)). Yet, such driver still could not explain the important sea-level
606 fluctuations observed, for example, during the Turonian Stage ([Haq et al., 1987](#); [Haq, 2014](#);
607 [Haq and Huber, 2016](#)), keeping glacio-eustasy the most plausible candidate (e.g., [Miller et
608 al., 2005b](#); [Boullila et al., 2011](#); [Ray et al., 2019](#); see also discussion in [Simmons et al., in
609 press](#)).

610 The above discussed eustatic drivers (thermo-eustasy, aquifer-eustasy and glacio-
611 eustasy) are all sensitive to orbitally forced climate. The 4.7 and 9.5 Myr orbital cycles
612 recorded in SL data ([Sections 5.2 and 5.3](#)) are also documented in deep-sea (benthic
613 foraminifera) stable carbon and oxygen isotopes, $\delta^{13}\text{C}$ and $\delta^{18}\text{O}$ ([Boullila et al., 2012](#); [Boullila,
614 2019](#)). Although the resolution of the Late Cretaceous isotopic data is low compared to that
615 in the Cenozoic, spectral analysis and filtering show evidence for 4.7 and 9.5 Myr cyclicities
616 in benthic $\delta^{18}\text{O}$ climate record along the past 100 Ma ([Boullila, 2019](#) his Figs. 1 and 2).

617

618 **6. Conclusions**

619 Integrated cyclostratigraphic and sequence stratigraphic study of the Late Cretaceous
620 Limoeiro Fm in the Foz do Amazonas Basin (offshore Brazil) allowed the detection of a rich
621 series of Milankovitch astronomical frequencies (100 kyr, 405 kyr, 2.4 Myr, 4.7 Myr and 9.5
622 Myr) together with a potential link between third- and second-order SL sequences, and long-
623 period orbital cycles.

624 Cyclostratigraphy was performed on gamma-ray (GR) well-log data in two wells: Well
625 44 dominated by deltaic deposits and Well 29 dominated by deltaic to distal marine deposits.

626 Time-series analysis of GR data shows similar Milankovitch cycle hierarchy in the two wells,
627 but a notable difference in amplitudes of the recorded cycles.

628 Long-period Milankovitch cyclicities (405 kyr, 2.4 Myr, 4.7 Myr and 9.5 Myr) were
629 detected with high fidelity in the two sites. The 405 kyr stable eccentricity cycle permits to
630 realize floating timescales for the two sites, and provides strong constraints on longer periods
631 of Milankovitch orbital forcing.

632 The 2.4 and 9.5 Myr cyclicities dominate in Well 29, while 4.7 and 9.5 Myr cyclicities
633 dominate in Well 44. We relate such differential orbital expression to different lithologies
634 between the two wells, one dominated by clays and silts (Well 29) and the other by clays and
635 sands (Well 44).

636 Sequence stratigraphy was based on seismic data especially those covering Well 44
637 because its location within a 3D seismic block conjointly with the good quality of reflectors.
638 The seismically mapped strong SL sequences closely match the 4.7 Myr orbital cycles
639 inferred from GR cyclostratigraphy. In addition, longer SL sequences were previously
640 interpreted in the Limoeiro Fm, and correspond to the 9.5 Myr orbital cycles detected in GR
641 data. The cyclostratigraphically detected orbital periods (405 kyr and 2.4 Myr), previously
642 ascribed to fourth- and third-order SL sequences, respectively, were not seismically captured
643 likely because of the low resolution of seismic data.

644 Accordingly, correlation of SL seismic sequences (fourth- to second-order) and long-
645 period Milankovitch cycles suggests important contribution of astronomical forcing to the
646 formation of SL depositional sequences. Fourth- and third-order SL sequences match
647 respectively 405 kyr and 2.4 Myr eccentricity cycles. Shorter second-order and suborder
648 sequences correlate to 4.7 and 9.5 Myr orbital cycles.

649 We hypothesize that even if tectonics may interfere at Myr to multi-Myr frequency
650 bands, the astroclimate signal strongly dominates and emerges in the sedimentary record at
651 multi-Myr timescales. Thus, our finding reassesses more important role to climate forcing in
652 SL sequences to the detriment of tectonics.

653

654

655 **Acknowledgments**

656 This study uses seismic and well-log data of the project IODP-CAPES "*Evolução*
657 *estratigráfica e estrutural da bacia da Foz do Amazonas: acoplamento entre processos*
658 *sedimentares, gravitacionais e de migração de fluidos*" sponsored By CAPES (Coordination
659 for the Improvement of Higher Level Education- Brazil). We greatly thank Agência Nacional
660 do Petróleo, Gás Natural e Biocombustíveis (ANP) that provided seismic and well-log data to
661 Universidade Federal Fluminense (UFF, Brazil) and Universidade do Estado de Rio de
662 Janeiro (UERJ, Brazil). Our special thanks are also due to CGG for providing 3D seismic grid

663 to Institut des Sciences de la Terre Paris (ISTeP, Sorbonne Université, CNRS, France). Slah
664 Boulila and Jacques Laskar were supported by French ANR Project AstroMeso. Alberto M.
665 Cruz was supported by IODP-CAPES project grant No. 0558/2015. Antonio Tadeu dos Reis
666 and Cleverson Guizan Silva received research grant No. 313086/2017-6 and No.
667 308164/2015-6 from the Brazilian National Research Council (CNPq). We are grateful to
668 Editor Massimo Zecchin, and thank the two reviewers for very helpful reviews that led to
669 important revisions of our manuscript.

670

671

672 **References**

- 673 Baker, P., Silva, C., Fritz, S., Reis, T., 2015. Deep drilling of the Amazon continental margin: The
674 evolution of Cenozoic neotropical biodiversity, climate, and oceanography. IODP Proposal.,
675 https://docs.iodp.org/Proposal_Cover_Sheets/859-Full2_Baker_cover.pdf.
- 676 Batenburg, S.J., Vleeschouwer, D.D., Sprovieri, M., Hilgen, F.J., Gale, A.S., Singer, B.S., Koeberl, C.,
677 Coccioni, R., Claeys, P., Montanari, A., 2016. Orbital control on the timing of oceanic anoxia in
678 the Late Cretaceous. *Clim. Past Discuss.* <https://doi.org/10.5194/cp-2015-182>.
- 679 Brandão, J.A.S.L., Feijó, F.J., 1994. Bacia da Foz do Amazonas: Boletim de Geociências da
680 Petrobras, 8, 1, p. 91–99.
- 681 Bornemann, A., Norris, R.D., Friedrich, O., Beckmann, B., Schouten, S., Damsté, J.S.S., Vogel, J.,
682 Hofmann, P., Wagner, T., 2008. Isotopic evidence for glaciation during the Cretaceous
683 Supergreenhouse. *Science* 319, 189–192.
- 684 Boulila, S., Galbrun, B., Hinnov, L.A., Collin, P.Y., Ogg, J.G., Fortwengler, D., Marchand, D., 2010.
685 Milankovitch and sub-Milankovitch forcing of the Oxfordian (Late Jurassic) Terres Noires
686 Formation (SE France) and global implications. *Basin Research* 22, 717–732.
- 687 Boulila, S., Galbrun, B., Huret, E., Hinnov, L.A., Rouget, I., Gardin, S., Bartolini, A., 2014.
688 Astronomical calibration of the Toarcian Stage: implications for sequence stratigraphy and
689 duration of the early Toarcian OAE. *Earth Planet. Sci. Lett.* 386, 98–111.
- 690 Boulila, S., Galbrun, B., Laskar, J., Pälike, H., 2012. A ~9 Myr cycle in Cenozoic $\delta^{13}\text{C}$ record and long-
691 term orbital eccentricity modulation. Is there a link? *Earth Planet. Sci. Lett.* 317-318, 273–281.
- 692 Boulila, S., Galbrun, B., Miller, K.G., Pekar, S.F., Browning, J.V., Laskar, J., Wright, J.D., 2011. On the
693 origin of Cenozoic and Mesozoic “third-order” eustatic sequences. *Earth-Sci. Rev.* 109, 94–112.
- 694 Boulila, S., Hinnov, L.A., Huret, E., Collin, P.Y., Galbrun, B., Fortwengler, D., Marchand, D., Thierry,
695 J., 2008. Astronomical calibration of the Early Oxfordian (Vocontian and Paris basins, France):
696 consequences of revising the Late Jurassic time scale. *Earth Planet. Sci. Lett.* 276, 40–51.
- 697 Boulila, S., Laskar, J., Haq, B.U., Galbrun, B., Hara, N., 2018a. Long-term cyclicities in Phanerozoic
698 sea-level sedimentary record and their potential drivers. *Glob. Planet. Ch.* 165, 128–136.
- 699 Boulila, S., Vahlenkamp, M., De Vleeschouwer, D., Laskar, J., Yamamoto, Y., Pälike, H., Kirtland
700 Turner, S., Sexton, P.F., Cameron, A., 2018b. Towards a robust and consistent middle Eocene
701 astronomical timescale. *Earth Planet. Sci. Lett.* 486, 94–107.

702 Boulila, S., 2019. Coupling between Grand cycles and Events in Earth's climate during the past 115
703 million years. *Scientific Reports*, doi: 10.1038/s41598-018-36509-7.

704 Burnett, J.A. 1998. Upper Cretaceous. In P.R. Bown (Ed.), *Calcareous Nannofossil Biostratigraphy*.
705 *British Micropaleontology Society Publications Series*, Kluwer Academic Publishers, London, p.
706 132–199.

707 Catuneanu, O., 2006. *Principles of Sequence Stratigraphy*. Elsevier, Amsterdam, 375p.

708 Catuneanu, O., 2019. Model-independent sequence stratigraphy. *Earth-Science Reviews* 188, 312–
709 388.

710 Christie-Blick, N., Mountain, G.S., Miller, K.G. 1990. Seismic stratigraphy: record of sea-level change.
711 In: Revelle, R. (Ed.) *Sea-level change*, National Research Council, Studies in Geophysics,
712 National Academy Press, 116–140.

713 Cleveland, W.S., 1979. Robust locally weighted regression and smoothing scatter plots. *J. Am. Stat.*
714 *Assoc.* 74, 829–836.

715 Cloetingh, S., 1988. Intraplate stresses: a tectonic cause for third-order cycles in apparent sea level?
716 *SEPM Spec. Publ.* 42, 19–29.

717 Cobbold, P.R., Mourgues, R. and Boyd, K., 2004. Mechanism of thin-skinned detachment in the
718 Amazon Fan: Assessing the importance of fluid overpressure and hydrocarbon generation.
719 *Marine and Petroleum Geology* 21, 1013–1025.

720 Cogné, J-P., Humler, E. 2006. Trends and rhythms in global seafloor generation rate. *Geochem.*
721 *Geophys. Geosyst.*, 7,Q03011, doi:10.1029/2005GC001148.

722 Cogné, J.P., Humler, E., Courtillot, V., 2006. Mean age of oceanic lithosphere drives eustatic sea-level
723 change since Pangea breakup. *Earth Planet. Sci. Lett.* 245, 115–122.

724 Crowley, J.W., Katz, R.F., Huybers, P., Langmuir, H.C., Sung-Hyun, P., 2015. Glacial cycles drive
725 variations in the production of oceanic crust. *Science* 347(6227), 1237–1240.

726 Cruz, A.M., 2018. Integrated geological and geophysical studies applied to understanding the
727 evolution of the Offshore Amazon Basin. PhD Thesis. Sorbonne Université, 223p.

728 Damuth, J., Embley, R., 1981. Mass transport processes on Amazon Cone: Western Atlantic Ocean.
729 *AAPG Bull.* 65, 629–643.

730 Damuth, J.E., Flood, R.D., Kowsmann, R.O., Belderson, R.H. and Gorini, M.A., 1988. Anatomy and
731 growth pattern of Amazon Deep-sea Fan revealed by long-range side-scan sonar (GLORIA) and
732 high resolution seismic studies. *AAPG Bulletin* 72, 885–911.

733 Damuth, J., Kumar, N., 1975. Amazon Cone: morphology, sediments, age, and growth pattern. *Geol.*
734 *Soc. Am. Bull.* 6, 863–878.

735 DeCelles, P.G., Ducea, M.N., Kapp, P., Zandt, G., 2009. Cyclicity in Cordilleran orogenic systems.
736 *Nat. Geosci.* 2, 251–257.

737 de Silva, S.L., Riggs, N.R., Barth, A.P., 2015. Quickening the pulse: fractal tempos in continental arc
738 magmatism. *Elements* 11,113–118.

739 Embry, S., Beauchamp, B., Dewing, K., Dixon, J., 2019. Episodic tectonics in the Phanerozoic
740 succession of the Canadian High Arctic and the “10-million-year flood”. in Piepjohn, K., Strauss,
741 J.V., Reinhardt, L. & McClelland, W.C., eds.: *Circum-Arctic Structural Events: Tectonic Evolution*

742 of the Arctic Margins and Trans-Arctic Links with Adjacent Orogens. Geological Society of
743 America Special Paper 541. doi.org/10.1130/2018.2541(11).

744 Figueiredo, J.J.P., Zalán, P.V. and Soares, E.F., 2007. Bacia da Foz do Amazonas: Boletim de
745 Geociencias da Petrobras, 15, 2, 299–309.

746 Friedrich, O., Norris, R.D., Erbacher, J., 2012. Evolution of middle to Late Cretaceous oceans—A 55
747 m.y. record of Earth's temperature and carbon cycle. *Geology* 40, 107–110.

748 Galeotti, S., Rusciadelli, G., Sprovieri, M., Lanci, L., Gaudio, A., Pekar, S., 2009. Sea-level control on
749 facies architecture in the Cenomanian–Coniacian Apulian margin (Western Tethys): A record of
750 glacio-eustatic fluctuations during the Cretaceous greenhouse? *Palaeogeography
751 Palaeoclimatology Palaeoecology* 276, 196–205.

752 Gorini, C., Haq, U.B., dos Reis, A.T, Silva, C.G., Cruz, A.M., Soares, E., Grangeon, D., 2013. Late
753 Neogene sequence stratigraphic evolution of the Foz do Amazonas Basin, Brazil. *Terra Nova* 26,
754 179–185.

755 Gornitz, V., Lebedeff, S., Hansen, J., 1992. Global sea-level trend in the past century. *Science* 215,
756 1611–1614.

757 Gradstein, F.M., Ogg, J.G., Schmitz, K., Ogg, G., 2012. *The Geologic Time Scale 2012*, vol. 2.
758 Elsevier. 1144 p.

759 Gradstein, F.M., Ogg, J.G., Smith, A.G., 2004. *A Geologic Time Scale 2004*. Cambridge University
760 Press, 589 p.

761 Haq, B.U., 2014. Cretaceous eustasy revisited. *Glob. Planet. Change*, 113, 44–58.

762 Haq, B.U., Hardenbol, J., Vail, P.R., 1987. Chronology of fluctuating sea levels since the Triassic.
763 *Science* 235, 1156–1167.

764 Haq, B.U., Hardenbol, J., Vail, P.R., 1988. Mesozoic and Cenozoic chronostratigraphy and cycles of
765 sea-level change. *SEPM* 42, 71–108.

766 Haq, B.U., Huber, B.T., 2016. Anatomy of a eustatic event during the Turonian (Late Cretaceous) hot
767 greenhouse climate. *Science China Earth Sciences* 60, 20–29, doi: 10.1007/s11430-016-0166-y.

768 Hays, J.D., Imbrie, J., Shackleton, N.J., 1976. Variations in the Earth's orbit: Pacemaker of the ice
769 ages. *Science* 194, 1121–1132.

770 Hilgen, F.J., 2010. Astronomical dating in the 19th century. *Earth-Science Reviews* 98, 65–80.

771 Hinnov, L.A., 2013. Cyclostratigraphy and its revolutionizing applications in the earth and planetary
772 sciences. *GSA Bulletin* 125 (11/12), 1703–1734.

773 Hinnov, L.A., Hilgen, F., 2012. Cyclostratigraphy and Astrochronology. In Gradstein, F.M., Ogg, J.G.,
774 Schmitz, K., Ogg, G. (2012) (Ed.), *The Geologic Time Scale 2012*, Elsevier, vol. 2, Chapter 4, p.
775 63–83.

776 Huber, B.T., MacLeod, K.G., Watkins, D.K., Coffin, M.F., 2018. The rise and fall of the Cretaceous Hot
777 Greenhouse climate. *Global and Planetary Change* 167, 1–23.

778 Huber, B.T., Norris, R.D., MacLeod, K.G., 2002. Deep-sea paleotemperature record of extreme
779 warmth during the Cretaceous. *Geology* 30, 123–126.

780 Huybers, P., Langmuir, C., 2009. Feedback between deglaciation, volcanism and atmospheric CO₂.
781 *Earth Planet. Sci. Lett.* 286, 479–491.

782 Jacobs, D.K., Sahagian, D.L., 1993. Climate-induced fluctuations in sea level during nonglacial times.
783 Nature 361, 710–712.

784 Jarvis, I., Lignum, J.S., Gröcke, D.R., Jenkyns, H.C., and Pearce, M.A., 2011. Black shale deposition,
785 atmospheric CO₂ drawdown, and cooling during the Cenomanian-Turonian Oceanic Anoxic
786 Event. *Paleoceanography* 26, PA3201.

787 Huang, Z., Boyd, R., O'Connell, S., 1992. Upper Cretaceous cyclic sediments from hole 762C,
788 Exmouth Plateau, Northwest Australia. In: Van Rad, U., Haq, B.U., et al. (Eds.), *Proc. Ocean
789 Drilling Program. Sci. Res*, vol. 122, pp. 259–277.

790 Huber, B.T., MacLeod, K.G., Watkins, D.K., Coffin, M.F., 2018. The rise and fall of the Cretaceous Hot
791 Greenhouse climate. *Global and Planetary Change* 167, 1–23.

792 Jenkyns, H.C., 2010. Geochemistry of oceanic anoxic events. *Geochemistry, Geophysics,
793 Geosystems* 11, Q03004, doi:10.1029/2009GC002788.

794 Kominz, M.A., Browning, J.V., Miller, K.G., Sugarman, P.J., Minzintseva, S., Scotese, C.R., 2008. Late
795 Cretaceous to Miocene sea-level estimates from the New Jersey and Delaware plain coreholes:
796 an error analysis. *Basin Research* 20, 211–226.

797 Kutterolf, S., Jegen, M., Mitrovica, J.X., Kwasnitschka, T., Freundt, A., Huybers, P.J., 2012. A
798 detection of Milankovitch frequencies in global volcanic activity. *Geology* 41, 227–230.

799 Laskar, J., 1990. The chaotic motion of the Solar System: a numerical estimate of the size of the
800 chaotic zone. *Icarus* 88, 266–291.

801 Laskar, J., Fienga, A., Gastineau, M., Manche, H., 2011. La2010: a new orbital solution for the long
802 term motion of the Earth. *Astron. Astrophys.* 532, A89. [https://doi.org/10.1051/0004-
803 6361/201116836](https://doi.org/10.1051/0004-6361/201116836).

804 Laskar, J., Robutel, P., Joutel, F., Gastineau, M., Correia, A.C.M., Levrard, B., 2004. A long-term
805 numerical solution for the insolation quantities of the Earth. *Astron. Astrophys.* 428, 261–285.

806 Lees, J.A., Bown, P.R., 2005. Upper Cretaceous calcareous nannofossil biostratigraphy, ODP Leg
807 198 (Shatsky Rise, northwest Pacific Ocean). In: Bralower, T.J. Premoli Silva, I. Malone, M.J.
808 (Ed.) *Proceedings of the Ocean Drilling Program, Scientific Results*, College Station, TX (Ocean
809 Drilling Program), 198, 1–60, <https://doi.org/10.2973/odp.proc.sr.198.114.2005>.

810 Liu, Z., Huang, C., Algeo, T.J., Liu, H., Hao, Y., Du, X., Lu, Y., Chen, P., Guo, L., Peng, L., 2018. High-
811 resolution astrochronological record for the Paleocene-Oligocene (66–23Ma) from the rapidly
812 subsiding Bohai Bay Basin, northeastern China. *Palaeogeogr. Palaeoclimatol. Palaeoecol.* 510,
813 78–92.

814 MacLeod, K.G., Huber, B.T., Berrocoso, Á.J., Wendler, I., 2013. A stable and hot Turonian without
815 glacial $\delta^{18}\text{O}$ excursions is indicated by exquisitely preserved Tanzanian foraminifera. *Geology*
816 41, 1083–1086.

817 Mann, M.E., Lees, J.M., 1996. Robust estimation of background noise and signal detection in climatic
818 time series. *Clim. Change* 33, 409–445.

819 Maslin, M., Mikkelsen, N., Vilela, C. and Haq, B.U., 1998. Sea-level and gas hydrate controlled
820 catastrophic sediment failures of the Amazon Fan. *Geology* 26, 1107–1110.

821 Matos, R.M.D., 2000. Tectonic Evolution of the Equatorial South Atlantic. *Atlantic Rift and Continental*
822 *Margins* 115, 331–354.

823 Matthews, R.K., 1984. Oxygen-isotopic record of ice-volume history: 100 million years of
824 glacioeustatic fluctuations. *AAPG Mem.* 36, 97–107.

825 Mayer, H., Appel, E., 1999. Milankovitch cyclicity and rock-magnetic signatures of paleoclimatic
826 changes in the Early Cretaceous Biancone Formation of the Southern Alps, Italy. *Cretac. Res.* 20,
827 189–214.

828 Mello, M.R., Koustoukos, E.A.M., Hart, M.B., Brassell, S.C. and Maxwell, J.R., 1989. Late
829 Cretaceous anoxic events in the Brazilian continental margin. *Organic Geochemistry* 14, 529–
830 542.

831 Mello, M.R., Mosmann, R., Silva, S.R.P., Maciel, R.R., Miranda, F.P., 2001. Foz do Amazonas area:
832 The last frontier for elephant hydrocarbon accumulations in the South Atlantic realm. In: M.W.,
833 Downey, J. C., Threet and W. A. Morgan, (ed.), *Petroleum provinces of the twenty-first century.*
834 *AAPG Memoir* 74, p. 403–414.

835 Mello, M. R., Telnaes, N. and Maxwell, J. R., 1995. The hydrocarbon source potential in the Brazilian
836 marginal basins: a geochemical and paleoenvironmental assessment. In: Huc, A.Y. (ed.),
837 *Paleogeography, Paleoclimate and Source Rocks.* AAPG, *Studies in Geology*, 40, p. 233–272.

838 Meyers, S.R., 2014. Astrochron: An R Package for Astrochronology (Available at).
839 cran.rproject.org/web/packages/astrochron/index.html.

840 Miller, K.G., Kominsz, M.A., Browning, J.V., Wright, J.D., Mountain, G.S., Katz, M.E., Sugarman, P.J.,
841 Cramer, B.S., Christie-Blick, N., Pekar, S.F., 2005a. The Phanerozoic record of global sea-level
842 change. *Science* 310, 1293–1298.

843 Miller, K.G., Lombardi, C.J., Browning, J.V., Schmelz, W.J., Gallegos, G, Mountain, G.S., Baldwin,
844 K.E. 2018. Back to basics of sequence stratigraphy: Early Miocene and mid-Cretaceous
845 examples from the New Jersey paleoshelf. *Journal of Sedimentary Research* 88, 148-176.

846 Miller, K.G., Wright, J.D., Browning, J.V., 2005b. Visions of ice sheets in a greenhouse world. *Marine*
847 *Geology* 217, 215-231.

848 Müller, R.D., Sdralias, M., Gaina, C., Steinberger, B., Heine, C., 2008. Long-term sea-level
849 fluctuations driven by ocean basin dynamics. *Science* 319, 1357–1362.

850 Myers, K.J., Milton, N.J. 1996. Concepts and principles of sequence stratigraphy. In: Emery, D.,
851 Myers, K.J. (Eds.) *Sequence Stratigraphy.* Blackwell, Oxford, 11-44.

852 Navarro-Ramirez, J.P., Bodin, S., Heimhofer, U., Immenhauser, A., 2015. Record of Albian to early
853 Cenomanian environmental perturbation in the eastern sub-equatorial Pacific. *Palaeogeogr.*
854 *Palaeoclimatol. Palaeoecol.* 423, 122–137.

855 Paillard, D., Labeyrie, L., Yiou, P, 1996. Macintosh program performs timeseries analysis. *Eos* 77,
856 379.

857 Pälike, H., Laskar, J., Shackleton, N.J., 2004. Geologic constraints on the chaotic diffusion of the Solar
858 System. *Geology* 32, 929–932.

859 Pälke, H., Norris, R.D., Herrle, J.O., Wilson, P.A., Coxall, H.K., Lear, C.H., Shackleton, N.J., Tripathi,
860 A.K., Wade, B.S., 2006. The Heartbeat of the Oligocene Climate System. *Science* 314, 1894–
861 1898.

862 Paul, C.R.C., Lamolda, M.A., Mitchell, S.F., Vaziri, M.R., Gorostidi, A., Marshall, J.D., 1999. The
863 Cenomanian-Turonian boundary at Eastbourne (Sussex, UK): a proposed European reference
864 section. *Palaeogeography, Palaeoclimatology, Palaeoecology* 150, 83–121.

865 Perovano, R., Reis, A.T. dos, Silva, C.G., Vendeville, B.C., Gorini, C., Oliveira, V. De, and Araújo, É.F.
866 da S., 2009, O Processo de Colapso Gravitacional da Seção Marinha da Bacia da Foz do
867 Amazonas - Margem Equatorial Brasileira: *Revista Brasileira de Geofísica*, v. 27, no. 3, p. 459–
868 484.

869 Posamentier, H.W., Vail, P.R., 1988. Eustatic controls on clastic deposition II—sequence and systems
870 tract models. In: Wilgus, C.K., Ross, C.A., Posamentier, H. (Eds.), *Sea-level Changes: An*
871 *Integrated Approach*. SEPM Special Publication, 42, 125–154.

872 Ray, D.C., van Buchem, F.S.P, Baines, G., Davies, A., Gréselle, B., Simmons, M.D., Robson, C.,
873 2019. The magnitude and cause of short-term eustatic Cretaceous sea-level change: A
874 synthesis. *Earth-Science Reviews* 197, 102901.

875 Reis, A.T., Araújo, E., Silva, C.G., Cruz, A.M., Gorini, C., Droz, L., Migeon, S., Perovano, R., King, I.,
876 and Bache, F., 2016, Effects of a regional décollement level for gravity tectonics on late Neogene
877 to recent large-scale slope instabilities in the Foz do Amazonas Basin, Brazil: *Marine and*
878 *Petroleum Geology*, doi: 10.1016/j.marpetgeo.2016.04.011.

879 Reis, A. T., Perovano, R., Silva, C.G., Vendeville, B.C., Araújo, E., Gorini, C., and Oliveira, V., 2010.
880 Two-scale gravitational collapse in the Amazon Fan: a coupled system of gravity tectonics and
881 mass-transport processes. *J. Geol. Soc. London* 167, 593–604, doi: 10.1144/0016-76492009-
882 035.

883 Sames, B., Wagreich, M., Wendler, J.E., Haq, B.U., Conrad, C.P., Melinte-Dobrinescu, M.C., Hu, X.,
884 Wendler, I., Wolfgring, E., Yilmaz, I.Ö., Zorina, S.O., 2016. Short-term sea-level changes in a
885 greenhouse world—A view from the Cretaceous. *Palaeogeography, Palaeoclimatology,*
886 *Palaeoecology* 441, 393–411.

887 Schulz, M., Schäfer-Neth, C., 1998. Translating Milankovitch climate forcing into eustatic fluctuations
888 via thermal deep water expansion: a conceptual link. *Terra Nova* 9, 228–231.

889 Schlanger, S.O., Jenkyns, H.C., 1976. Cretaceous oceanic anoxic events: causes and consequences.
890 *Geol. Mijnb.* 55, 179–184.

891 Silva, C.G., Araújo, E.F.S., Reis, A.T., Perovano, R., Gorini, C., Vendeville, B.C., Albuquerque, N.C.
892 2010. Megaslides in the Foz do Amazonas Basin, Brazilian Equatorial Margin. In: *Submarine*
893 *Mass Movements and Their Consequences* (D.C. Mosher, R.C. Shipp, L. Moscardelli, J.D.
894 Chaytor, C.D.P. Baxter, H.J. Lee and R. Urgeles, eds). *Adv. Nat. Technol Hazards* 28, 581– 591.
895 Springer - Verlag, New York.

896 Silva, S.R.P., Maciel, R.R., Severino, M.C.G., 1999. Cenozoic tectonics of Amazon Mouth Basin. *Geo-*
897 *Marine Letters* 18, 256–262.

- 898 Simmons, M.D., 2012. Sequence Stratigraphy and Sea-Level Change. In: Gradstein, F.M., Ogg, J.G.,
899 Schmitz, M.D., Ogg, G.M. (Eds.) *The Geologic Time Scale 2012*, v.1, pp. 239–267.
- 900 Simmons, M.D., Miller, K.G., Ray, D.C., Davies, A., van Buchem, F.S.P, Gréselle, B., in press.
901 Phanerozoic eustasy. In: Gradstein, F.M., Ogg, J.G., Schmitz, M.D., Ogg, G.M. (Eds.) *The*
902 *Geologic Time Scale 2020*, v.x, pp. xxx–xxx.
- 903 Sprovieri, M., Sabatino, N., Pelosi, N., Batenburg, S.J., Coccioni, R., Iavarone, M., Mazzola, S., 2013,
904 2013. Late Cretaceous orbitally-paced carbon isotope stratigraphy from the Bottaccione Gorge
905 (Italy). *Palaeogeogr. Palaeoclim. Palaeoecol.* 379–380, 81–94.
- 906 Stoll, H.M., Schrag, D.P., 1996. Evidence for glacial control of rapid sea level changes in the Early
907 Cretaceous. *Science* 272, 1771–1774.
- 908 Stoll, H.M., Schrag, D.P., 2000. High-resolution stable isotope records from the Upper Cretaceous
909 rocks of Italy and Spain: Glacial episodes in a greenhouse planet? *Geological Society of America*
910 *Bulletin* 112, 308–319.
- 911 Strasser, A., Pittet, B., Hillgärtner, H., Pasquier, J.B., 1999. Depositional sequences in shallow
912 carbonate-dominated sedimentary systems: concepts for a high-resolution analysis. *Sedimentary*
913 *Geology* 128, 201–221.
- 914 Strasser, A., Hillgärtner, H., Hug, W., Pittet, B., 2000. Third-order depositional sequences reflecting
915 Milankovitch cyclicity. *Terra Nova* 12, 303–311.
- 916 Thomson, D.J., 1982. Spectrum estimation and harmonic analysis. *IEEE Proc.*70, 1055–1096.
- 917 Tsikos, H., Karakitsios, V., van Breugel, Y., Walsworth-Bell, B., Bombardiè, L., Petrizzo, M.R.,
918 Sinninghe Damsté, J.S., Schouten, S., Erba, E., Premoli Silva, I., Farrimond, P., Tyson, R.V.,
919 Jenkyns, H.C., 2004. Organic carbon deposition in the Cretaceous of the Ionian Basin, NW
920 Greece: The Paquier event (OAE1b) revisited. *Geological Magazine* 141, 401–416.
- 921 Vail, P.R., Mitchum, R.M., Todd, J.R.G., Widmier, J.M., Thompson, S., Sangree, J.B., Bubb, J.N.,
922 Hatlelid, W.G., 1977. In: Payton, C.E. (Ed.), *Seismic stratigraphy and global changes of sea level:*
923 *Seismic Stratigraphy – Applications to Hydrocarbon Exploration*. Mem. Am. Ass. Pertol. Geol. 26,
924 pp. 49–212.
- 925 Wagreich, M., Lein, R., Sames, B., 2014. Eustasy, its controlling factors, and the limn-eustatic
926 hypothesis – concepts inspired by Eduard Suess. *Austrian Journal of Earth Sciences* 107, 115-
927 131.
- 928 Weedon, G.P., Coe, A.L., Gallois, R.W., 2004. Cyclostratigraphy, orbital tuning and inferred
929 productivity for the type Kimmeridge Clay (Late Jurassic), Southern England. *Journal of the*
930 *Geological Society* 161, 655–666.
- 931 Wendler, J.E., Wendler, I., Vogt, C., Kuss, J. 2016. Link between cyclic eustatic sea-level change and
932 continental weathering: evidence for aquifer-eustasy in the Cretaceous. *Palaeogeography,*
933 *Palaeoclimatology, Palaeoecology* 441, 430-437.
- 934 Wilson, P.A., Norris, R.D., 2001. Warm tropical ocean surface and global anoxia during the mid-
935 Cretaceous period. *Nature* 412, 425–429.

936 Wolfram, L.C., Weinberg, R.F., Nebel, O., Hamza, K., Hasalová, P., Míková, J., Becchio, R., 2019. A
 937 60-Myr record of continental back-arc differentiation through cyclic melting. *Nat. Geosci.* 12, 215–
 938 219.

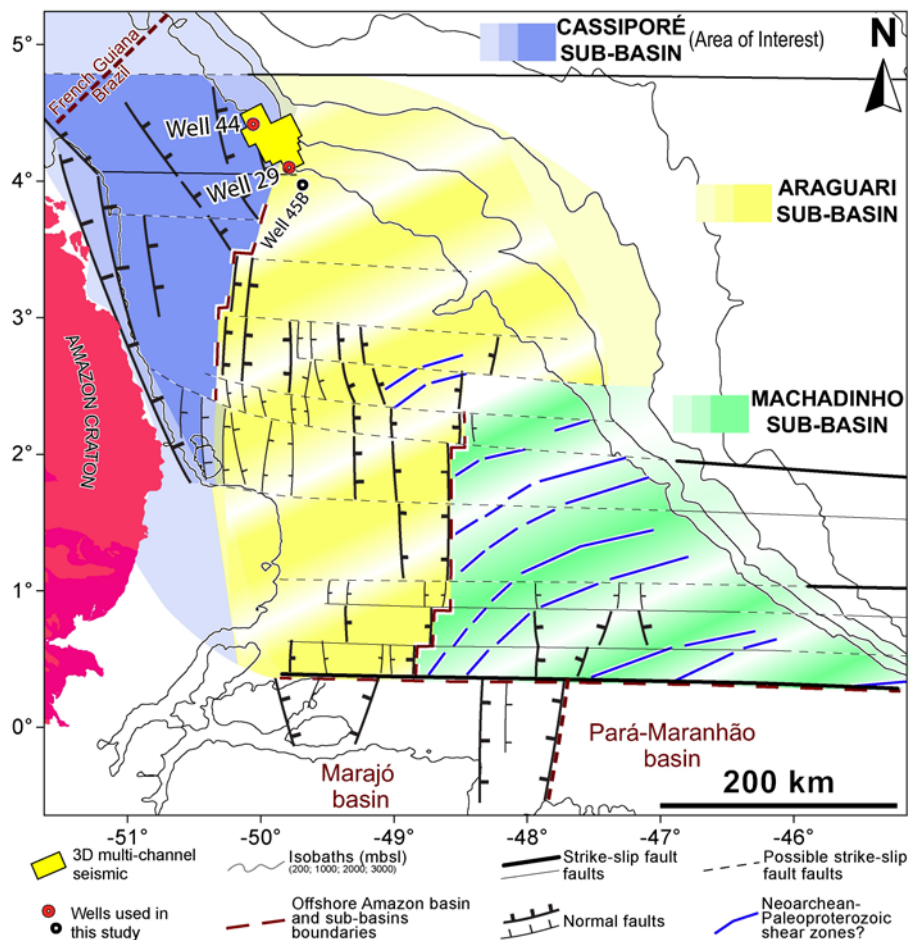
939 Wu, H., Zhang, S., Jiang, G., Hinnov, L., Yang, T., Li, H., Wan, X. and Wang, C., 2013.
 940 Astrochronology of the Early Turonian–Early Campanian terrestrial succession in the Songliao
 941 Basin, northeastern China and its implication for long-period behavior of the Solar System.
 942 *Palaeogeogr. Palaeoclimatol. Palaeoecol.* 385, 55–70.

943

944

945 **Figures and tables captions**

946



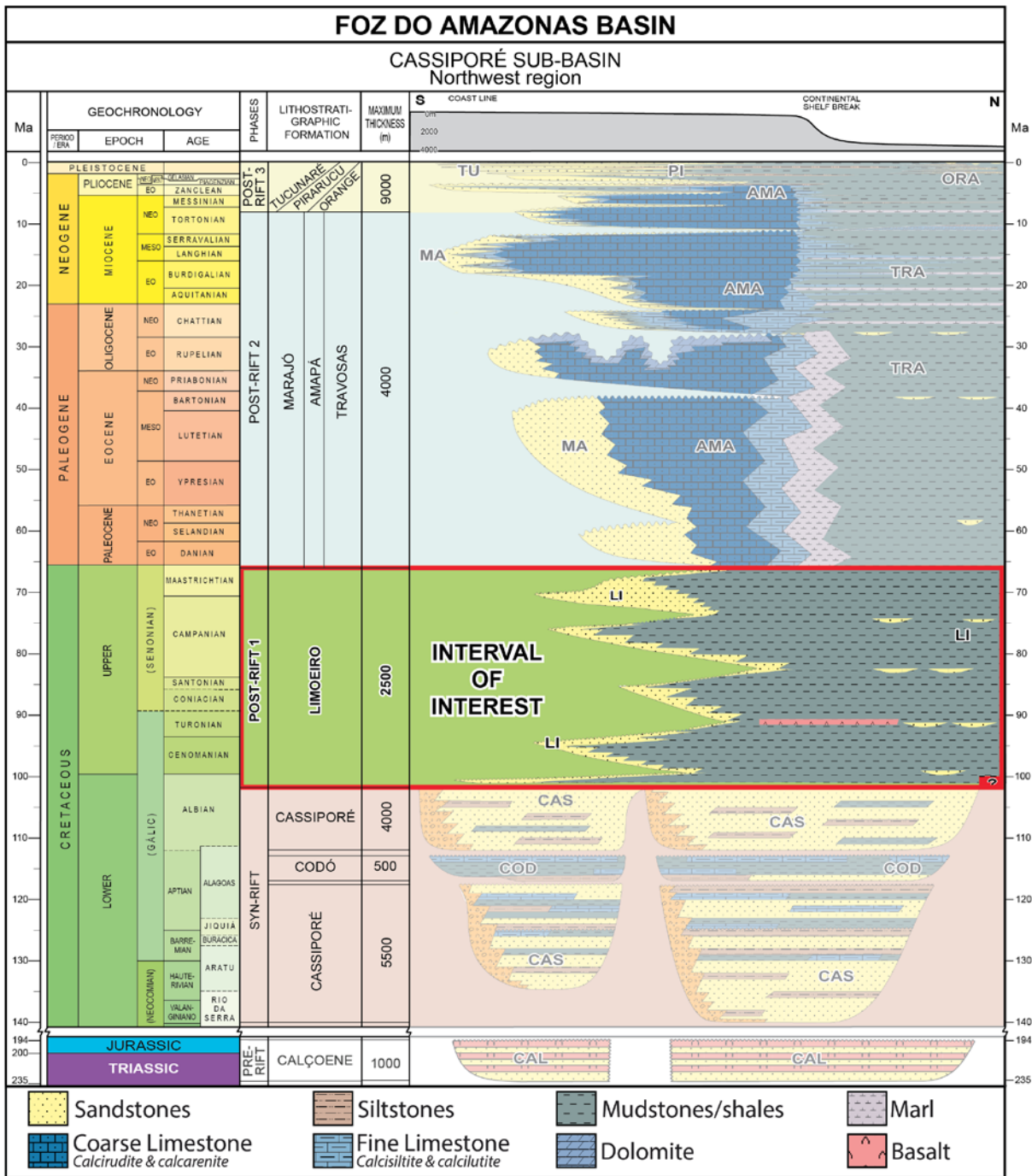
947

948 **Figure 1:** Simplified structural framework of the Foz do Amazonas Basin based on an
 949 integrated study of seismic reflection and potential field data (Cruz, 2018). The three studied
 950 petroleum wells 1-APS-29-AP, 1-APS-44-AP and 1-APS-45B-AP (indicated as 29, 44 and
 951 45B). Well 45B is used only for biostratigraphic data because it captures only the top of the
 952 Limoeiro Fm (see Fig. SI-7).

953

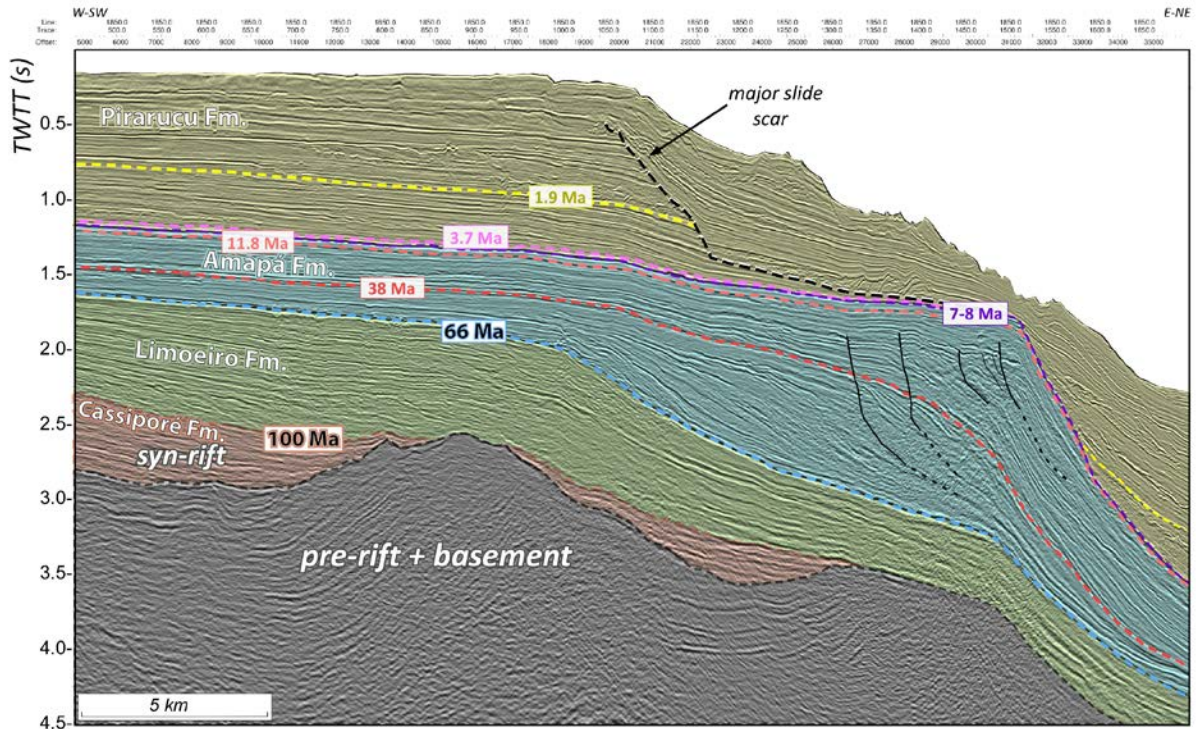
954

955



956
957
958
959
960
961
962

Figure 2: Stratigraphic chart of the Cassiporé Sub-basin (NW Amazon Margin); red box highlights the stratigraphic interval investigated in this study, dashed lines indicate the three post-rift megasequences (modified from Cruz, 2018). Late Cretaceous to Triassic based on Figueiredo et al. (2007), and age calibration of Limoeiro Fm according to the present study.



963

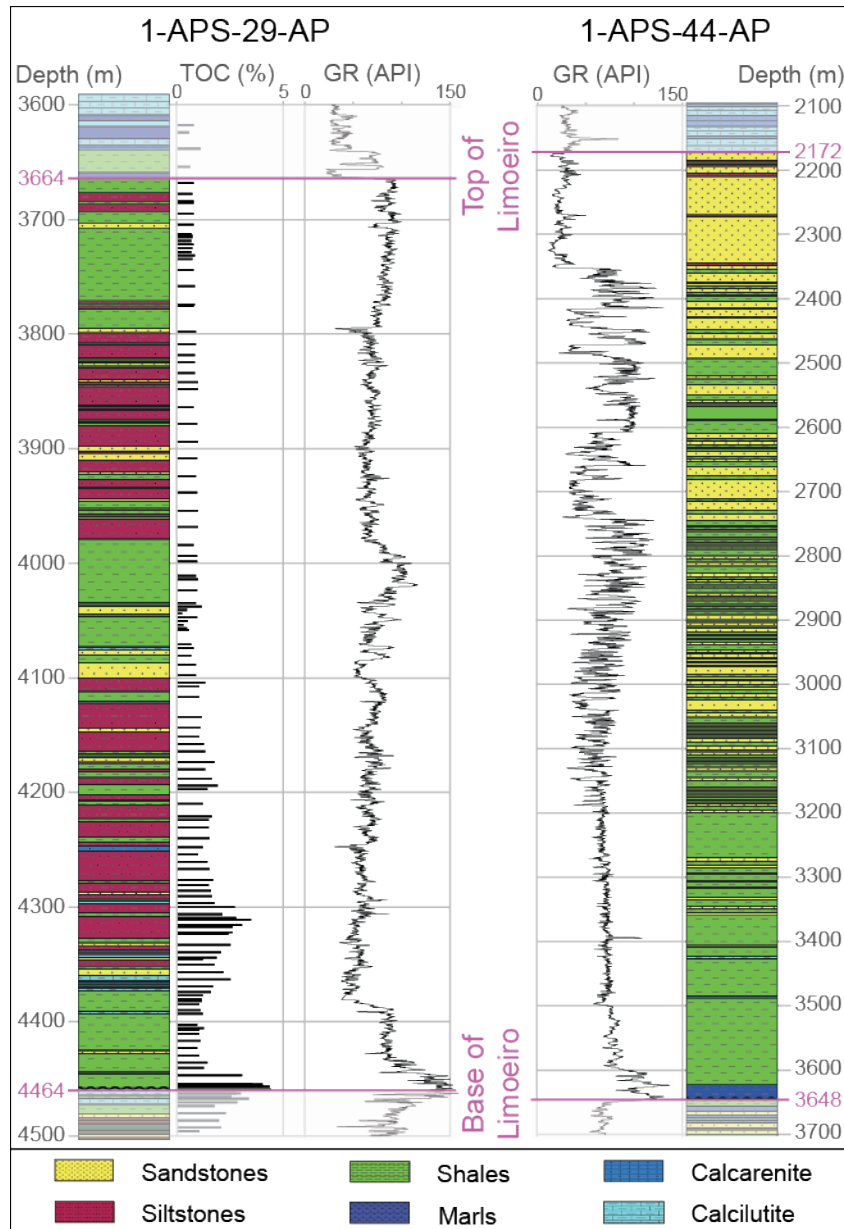
964 **Figure 3:** Interpreted seismic profile across NW Amazon Margin (Cassiporé Sub-basin)
 965 showing the basement and pre-rift strata, overlain by syn-rift Cassiporé Fm (orange), and
 966 post-rift Limoeiro (green), Amapá (blue) and Pirarucu (yellow) Formations (modified from
 967 [Baker et al., 2015](#); [Cruz, 2018](#)) .

968

969

970

971



972

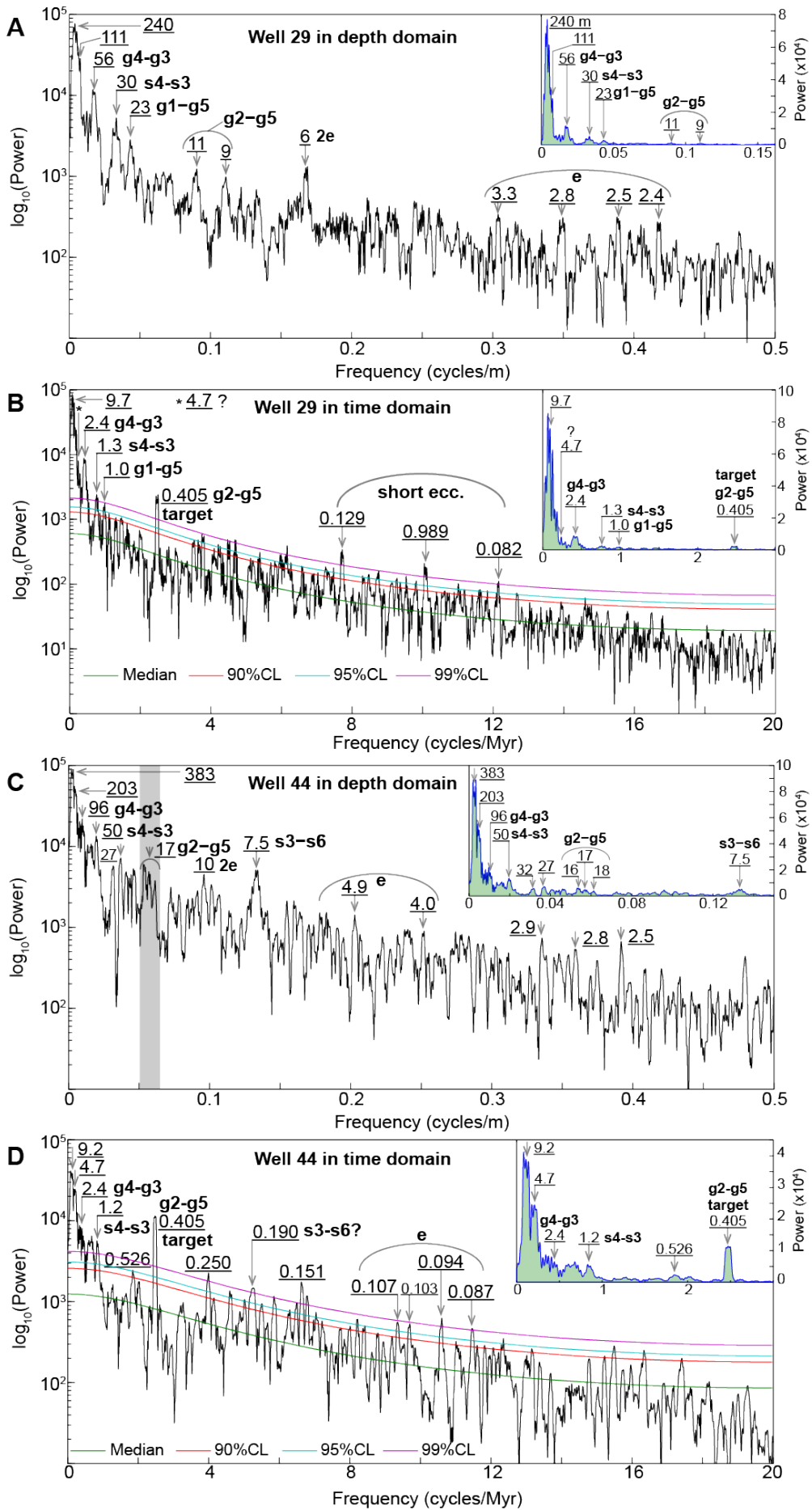
973

974 **Figure 4:** Lithostratigraphy and gamma-ray (GR) log data of the Limoeiro Fm in Wells 29 and

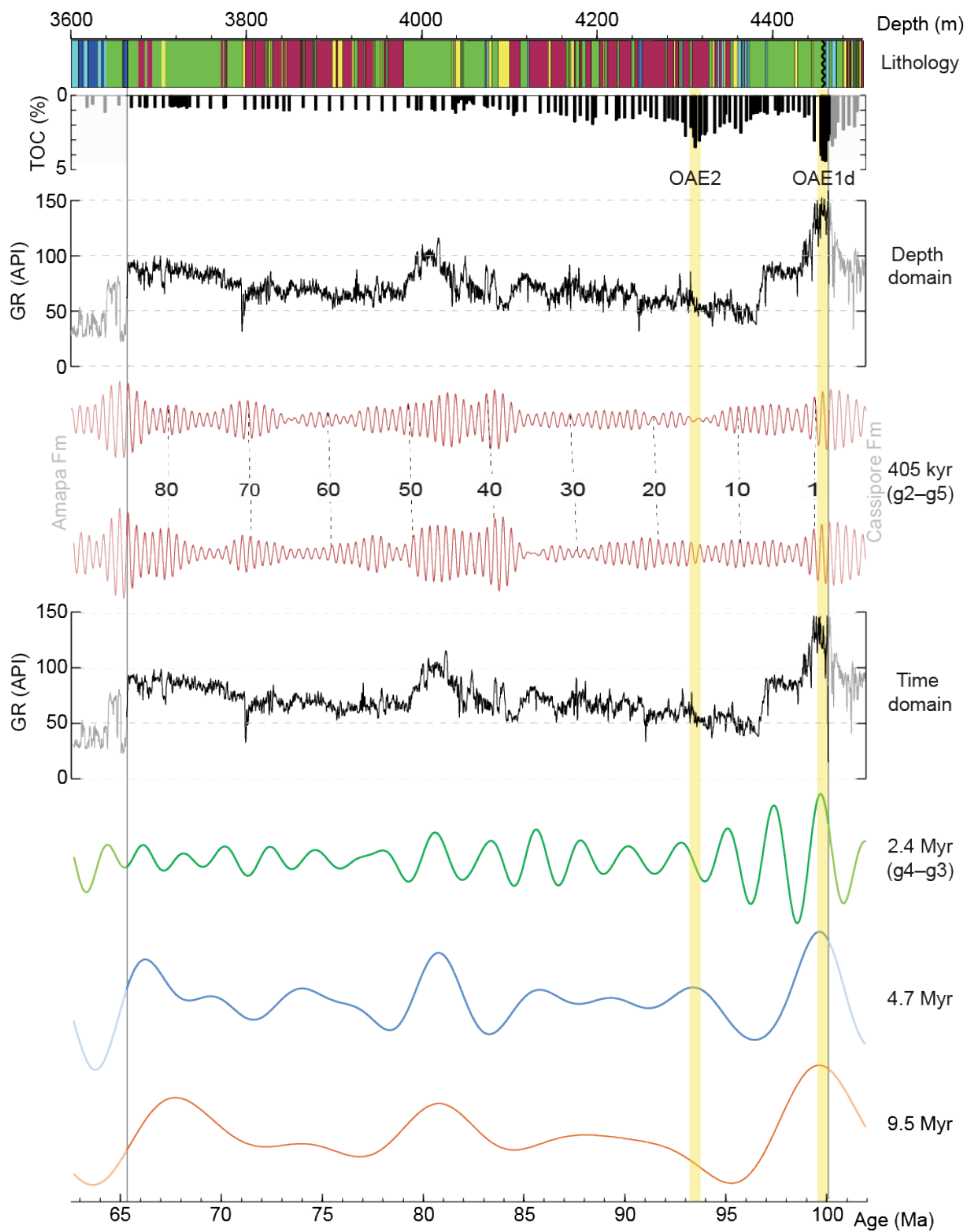
975 44, and Total Organic Carbon (TOC) data in Well 29.

976

977

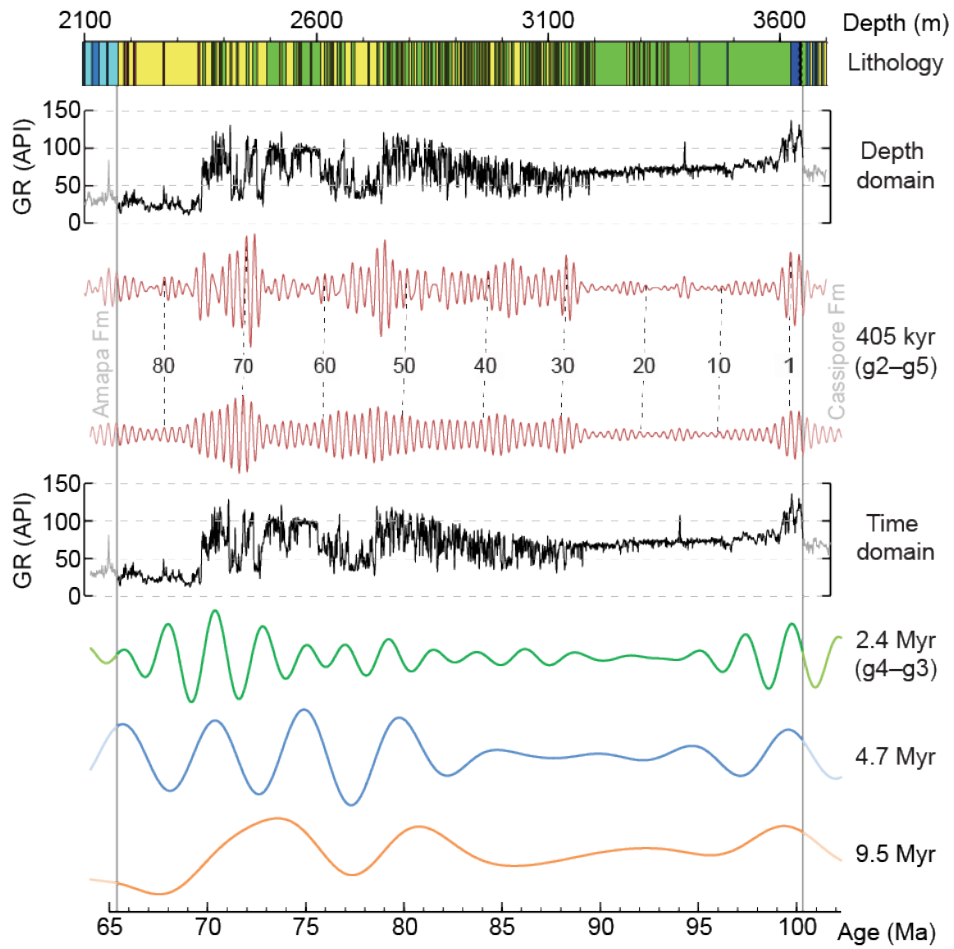


979 **Figure 5:** 2π -MTM power spectra of untuned (A and C) and tuned (B and D) GR data of the
980 Limoeiro Fm equivalent interval in Well 29 (3400-4580 m) and Well 44 (2045-3725 m). **(A)**
981 Spectrum of 35% weighted average detrended GR data in Well 29. *Inset:* Spectrum in a
982 linear scale power axis together with truncated frequency axis at 0.16 cycles/m. **(B)**
983 Spectrum of the raw GR data in Well 29. *Inset:* Spectrum in a linear scale power axis
984 together with truncated frequency axis at 3 cycles/Myr. **(C)** Spectrum of 35% weighted
985 average detrended GR data in Well 44. *Inset:* Spectrum in a linear scale power axis together
986 with truncated frequency axis at 0.15 cycles/m. **(D)** Spectrum of 35% weighted average
987 detrended GR data in Well 44. *Inset:* Spectrum in a linear scale power axis together with
988 truncated frequency axis at 3 cycles/m.
989



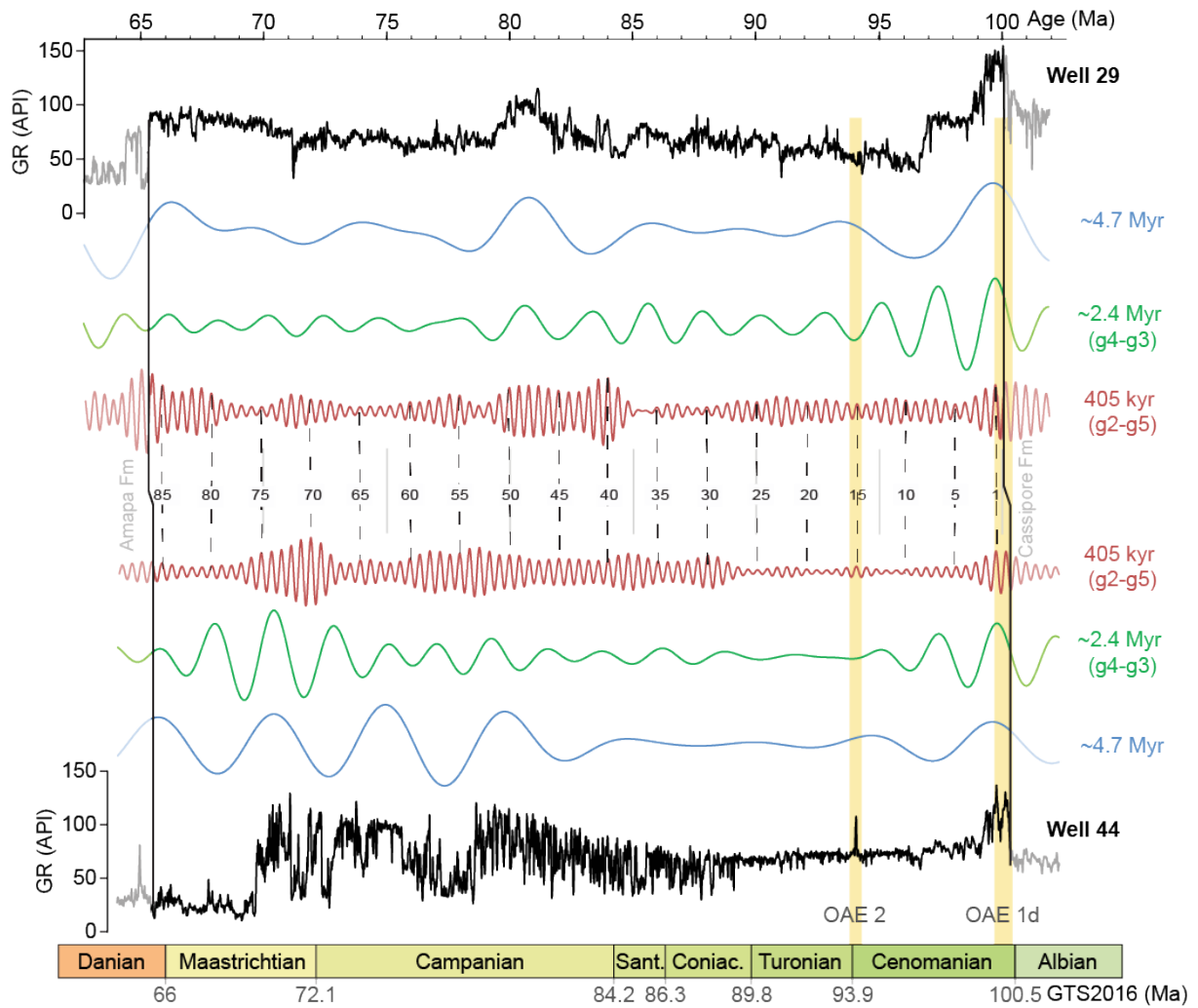
990
 991
 992
 993
 994

Figure 6: Astronomical age model of the Limoeiro Fm in Well 29 along with bandpass filtering of long-period Milankovitch cycles (405 kyr, 2.4, 4.7 and 9.5 Myr orbital cycles).



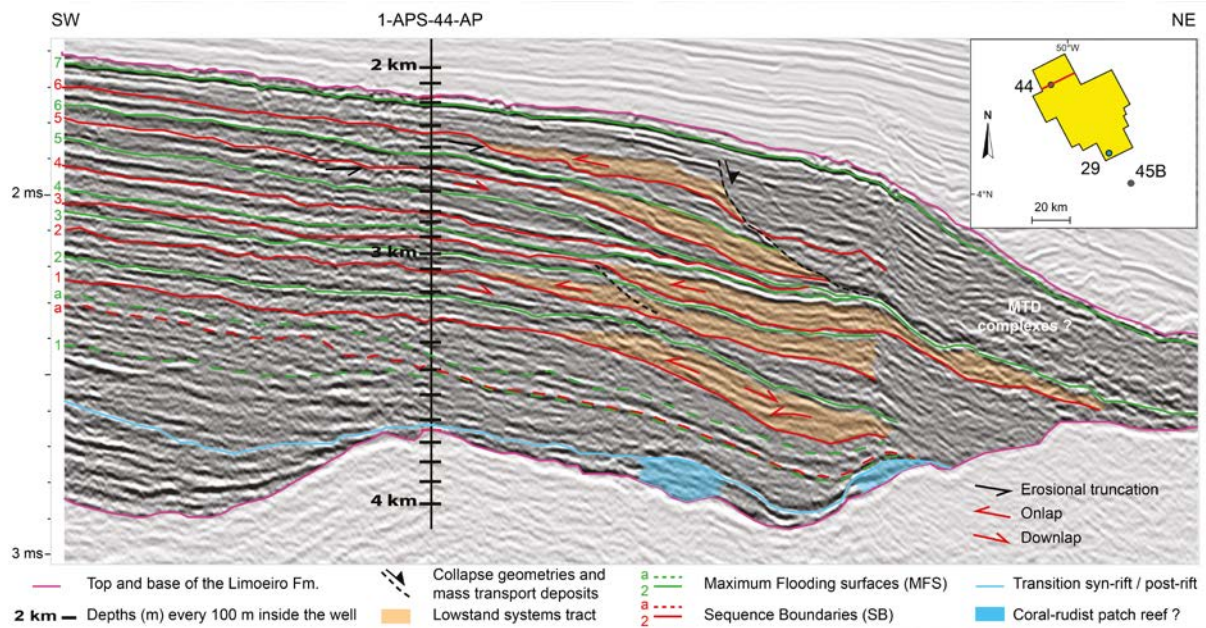
995
 996
 997
 998
 999

Figure 7: Astronomical age model of the Limoeiro Fm in Well 44 along with bandpass filtering of long-period Milankovitch cycles (405 kyr, 2.4, 4.7 and 9.5 Myr orbital cycles).



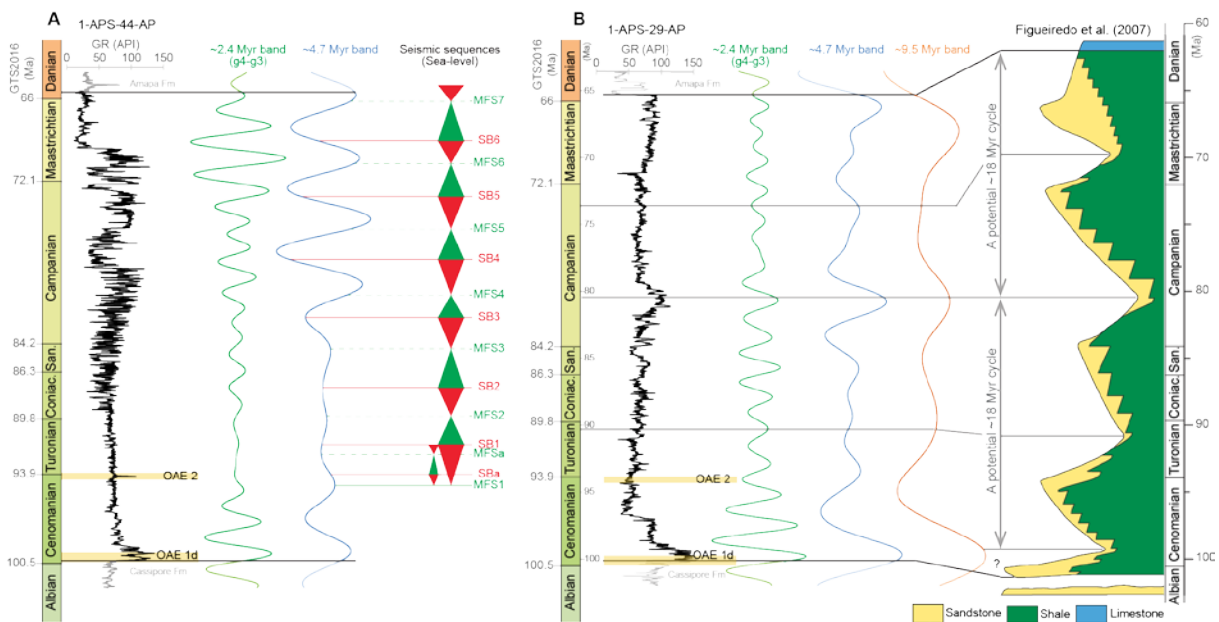
1000
 1001
 1002
 1003
 1004
 1005
 1006

Figure 8: Correlation of astronomical age models of the Limoeiro Fm in Well 29 versus Well 44, along with bandpass filtering of long-period Milankovitch cycles (405 kyr, 2.4, 4.7 Myr orbital cycles).



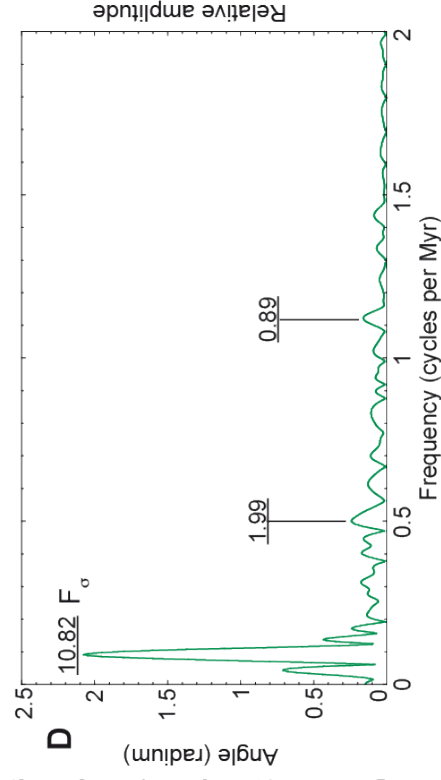
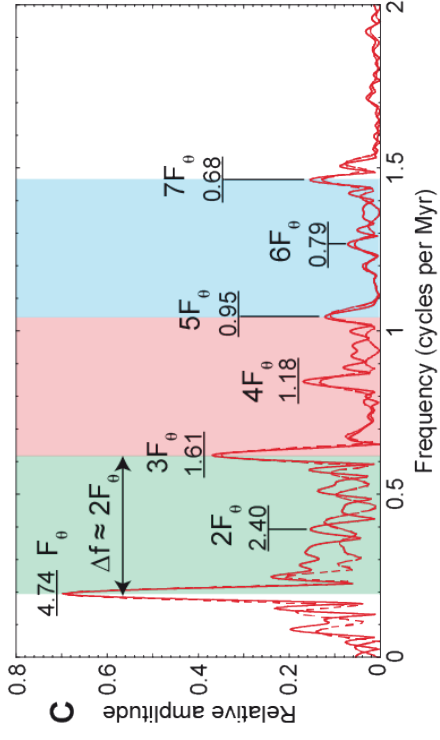
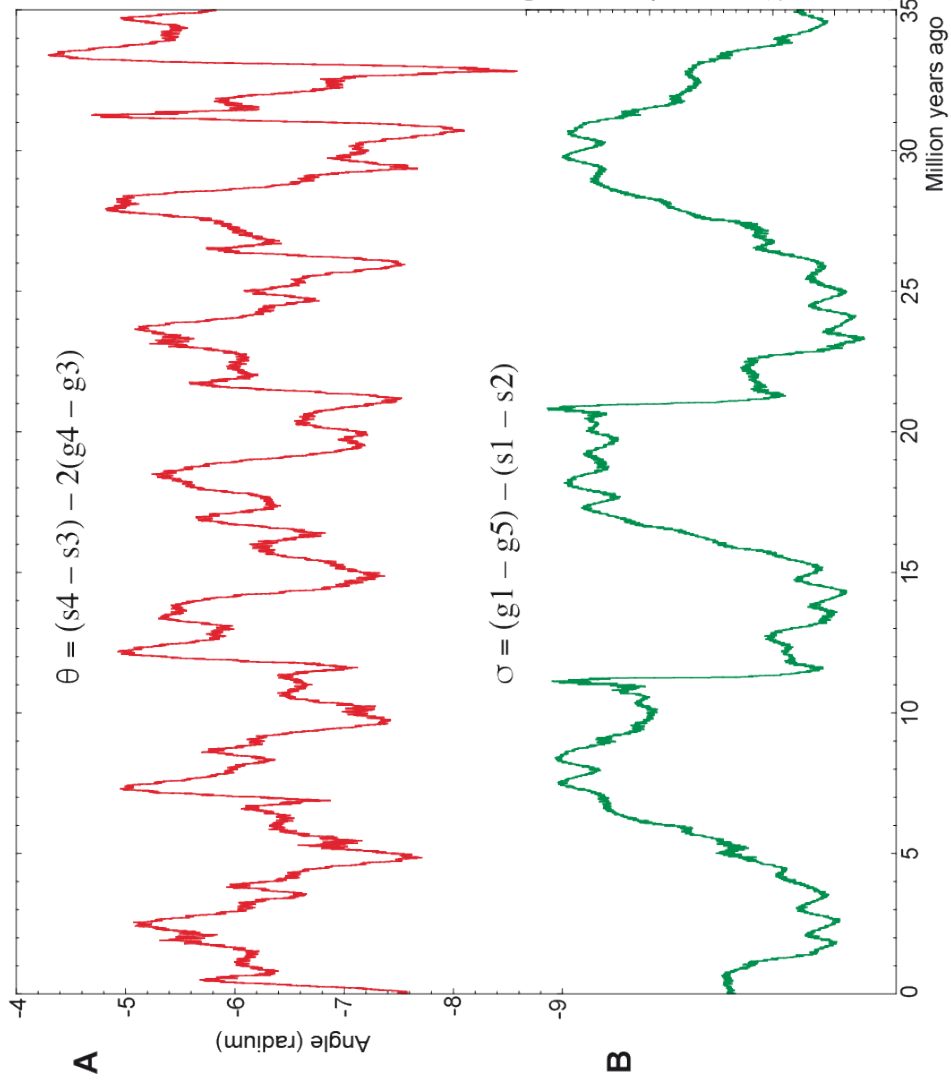
1007
1008
1009
1010
1011

Figure 9: Seismic interpretation of the Limoeiro Fm in the inline crossing Well 44 from 3D seismic data.



1012
1013
1014
1015
1016
1017
1018
1019
1020

Figure 10: Correlation of 4.7 and 9.5 Myr orbitally related cycles inferred from GR cyclostratigraphy, and main SL sequences inferred from seismic data and previous studies. **(A)** Correlation of 4.7 Myr orbital cycles with seismically detected second-order SL sequences in Well 44. **(B)** Correlation of 9.5 Myr orbital cycles in Well 29 with the main SL sequences that compose the Limoeiro Fm (Figueiredo et al., 2007).



1022 **Figure 11:** Harmonic analysis of the resonant arguments θ and σ over the past 35 Ma. **(A)**
1023 Variations of θ . **(B)** Variations of σ . **(C)** 2pi-MTM amplitude spectrum of θ . Fundamental
1024 libration frequency ' $F\theta$ ' and its harmonics ($3F\theta$, $5F\theta$ and $7F\theta$) are indicated by shaded areas.
1025 **(D)** 2pi-MTM amplitude spectrum of σ , the main peak represents the fundamental libration
1026 frequency ' $F\sigma$ '.
1027
1028

Earth's orbital parameters	Interfering terms (periods in kiloyear)	Resulting long periods (associated to θ or σ)
Climatic precession	$p + g_3 \approx 19.1$ $p + g_4 \approx 18.9$	$g_4 - g_3 \approx 2.4$ Myr (θ)
	$p + g_1 \approx 23.1$ $p + g_5 \approx 23.6$	$g_1 - g_5 \approx 1$ Myr (σ)
	$p + g_4 \approx 18.94$ $p + g_{n6} \approx 19.29$	$g_4 - g_{n6} \approx 1.6$ Myr (θ)
	$p + g_3 \approx 19.07$ $p + g_{n7} \approx 19.29$	$g_3 - g_{n7} \approx 4.7$ Myr (θ)
Obliquity	$p + s_1 \approx 28.8$ $p + s_2 \approx 29.8$	$s_1 - s_2 \approx 0.9$ Myr (σ)
	$p + s_3 \approx 40.8$ $p + s_4 \approx 39.4$	$s_4 - s_3 \approx 1.2$ Myr (θ)
	$p + v_{10} \approx 41.5$ $p + s_3 \approx 40.8$	$s_3 - v_{10} \approx 2.4$ Myr (θ)
	$p + v_{20} \approx 40.06$ $p + s_4 \approx 39.4$	$s_4 - v_{20} \approx 2.4$ Myr (θ)
Eccentricity	$g_4 - g_5 \approx 94.9$ $g_3 - g_5 \approx 98.8$	$g_4 - g_3 \approx 2.4$ Myr (θ)
	$g_4 - g_2 \approx 123.7$ $g_3 - g_2 \approx 130.8$	$g_4 - g_3 \approx 2.4$ Myr (θ)
	$g_2 - g_5 \approx 405$ $(g_2 - g_5) + (g_4 - g_3) \approx 346$	$g_4 - g_3 \approx 2.4$ Myr (θ)
	$g_2 - g_5 \approx 405$ $(g_2 - g_5) - (g_4 - g_3) \approx 490$	$g_4 - g_3 \approx 2.4$ Myr (θ)
	$g_4 - g_3 \approx 2361$ ($2F_\theta$) $g_4 - g_{n6} \approx 1624$ ($3F_\theta$)	$g_3 - g_{n6} \approx 4.7$ Myr (θ)
	$g_4 - g_3 \approx 2361$ ($2F_\theta$) $g_3 - g_{n7} \approx 4700$ (F_θ)	$g_4 - g_{n7} \approx 4.7$ Myr (θ)

1029
1030
1031 **Table 1:** Possible interfering terms of Earth's orbital parameters (climatic precession,
1032 obliquity and eccentricity) and the resulting long-period cyclicities associated with the main
1033 resonant arguments $\theta = 2(g_4 - g_3) - (s_4 - s_3)$ and $\sigma = (g_1 - g_5) - (s_1 - s_2)$. ' p ' is the Earth's
1034 axial precession (present-day value: 50.4758 arcsec/yr, [Laskar et al., 2004](#)) and ' g_i ' and ' s_i '
1035 are the secular frequencies as in [Table SIII-1](#). ' $F\theta$ ' is the fundamental libration frequency
1036 related to the argument θ (see '[Section 5.2](#)' for detail). v_{10} and v_{20} are two higher order terms

1037 of $s_3 - (g_4 - g_3)$ and $s_4 - (g_4 - g_3)$, respectively. g_{n6} and g_{n7} are $g_3 - F\theta$ and $g_3 + F\theta$,
 1038 respectively.

1039

1040

Order	Suborder	Mean period (Myr)	Causal mechanism	Astronomy
First	Longer	250-300*	Tectonic, galactic?	Radial motion?
	Shorter	91*	Tectonic, galactic?	
Second	Longer	36*	Tectonic, galactic?	Vertical motion?
	Medium-2	18	Tectonic, Milankovitch?	
	Medium-1	9.5	Milankovitch?	Eccentricity-Obliquity?
	Shorter	4.7	Milankovitch	Eccentricity-Obliquity
Third	Longer	2.4	Milankovitch	Eccentricity (g_4-g_3)
	Shorter	1.2	Milankovitch	Obliquity (s_4-s_3)
Fourth		0.405	Milankovitch	Eccentricity (g_2-g_5)
Fifth	Longer	0.173	Milankovitch	Obliquity
	Shorter	0.1	Milankovitch	Eccentricity
Sixth	Longer	0.04	Milankovitch	Obliquity
	Shorter	0.020	Milankovitch	Precession

1041

1042

1043 **Table 2:** Updated SL sequence hierarchy and causal mechanisms. Bold text indicates the
 1044 updates. The remaining are as in a review by [Boulila et al. \(2011, 2018a\)](#). * Phanerozoic
 1045 mean periodicity.

Earth's orbital parameters	Interfering terms (periods in kiloyear)	Resulting long periods (associated to θ or σ)
Climatic precession	$p + g_3 \approx 19.1$ $p + g_4 \approx 18.9$	$g_4 - g_3 \approx 2.4$ Myr (θ)
	$p + g_1 \approx 23.1$ $p + g_5 \approx 23.6$	$g_1 - g_5 \approx 1$ Myr (σ)
	$p + g_4 \approx 18.94$ $p + g_{n6} \approx 19.29$	$g_4 - g_{n6} \approx 1.6$ Myr (θ)
	$p + g_3 \approx 19.07$ $p + g_{n7} \approx 19.29$	$g_3 - g_{n7} \approx 4.7$ Myr (θ)
Obliquity	$p + s_1 \approx 28.8$ $p + s_2 \approx 29.8$	$s_1 - s_2 \approx 0.9$ Myr (σ)
	$p + s_3 \approx 40.8$ $p + s_4 \approx 39.4$	$s_4 - s_3 \approx 1.2$ Myr (θ)
	$p + v_{10} \approx 41.5$ $p + s_3 \approx 40.8$	$s_3 - v_{10} \approx 2.4$ Myr (θ)
	$p + v_{20} \approx 40.06$ $p + s_4 \approx 39.4$	$s_4 - v_{20} \approx 2.4$ Myr (θ)
Eccentricity	$g_4 - g_5 \approx 94.9$ $g_3 - g_5 \approx 98.8$	$g_4 - g_3 \approx 2.4$ Myr (θ)
	$g_4 - g_2 \approx 123.7$ $g_3 - g_2 \approx 130.8$	$g_4 - g_3 \approx 2.4$ Myr (θ)
	$g_2 - g_5 \approx 405$ $(g_2 - g_5) + (g_4 - g_3) \approx 346$	$g_4 - g_3 \approx 2.4$ Myr (θ)
	$g_2 - g_5 \approx 405$ $(g_2 - g_5) - (g_4 - g_3) \approx 490$	$g_4 - g_3 \approx 2.4$ Myr (θ)
	$g_4 - g_3 \approx 2361$ ($2F_\theta$) $g_4 - g_{n6} \approx 1624$ ($3F_\theta$)	$g_3 - g_{n6} \approx 4.7$ Myr (θ)
	$g_4 - g_3 \approx 2361$ ($2F_\theta$) $g_3 - g_{n7} \approx 4700$ (F_θ)	$g_4 - g_{n7} \approx 4.7$ Myr (θ)

Order	Suborder	Mean period (Myr)	Causal mechanism	Astronomy
First	Longer	250-300*	Tectonic, galactic?	Radial motion?
	Shorter	91*	Tectonic, galactic?	
Second	Longer	36*	Tectonic, galactic?	Vertical motion?
	Medium-2	18	Tectonic, Milankovitch?	
	Medium-1	9.5	Milankovitch?	Eccentricity-Obliquity?
Third	Shorter	4.7	Milankovitch	Eccentricity-Obliquity
	Longer	2.4	Milankovitch	Eccentricity (g4-g3)
	Shorter	1.2	Milankovitch	Obliquity (s4-s3)
Fourth		0.405	Milankovitch	Eccentricity (g2-g5)
Fifth	Longer	0.173	Milankovitch	Obliquity
	Shorter	0.1	Milankovitch	Eccentricity
Sixth	Longer	0.04	Milankovitch	Obliquity
	Shorter	0.020	Milankovitch	Precession